TECHNISCHE UNIVERSITÄT WIEN
Vienna | Austria

Diploma Thesis

Comparison of Subchondral Bone Stresses with Physiological and Simplified Articular Loading of the Radiocarpal Joint Using Finite Element Analysis

carried out for the purpose of obtaining the degree of Master of Science (Dipl.-Ing.) submitted at the TU Wien Faculty of Mechanical and Industrial Engineering by

Laurenz Berger
Mat.Nr.: 01626529
Liebhartstalstraße 33A
1160 Wien

under supervision of:
Univ.Prof. Dipl.-Ing. Dr.techn. Dieter Pahr
Dipl.-Ing. Dr.techn. Alexander Synek, MSc.
Institute of Lightweight Design and Structural Biomechanics (E317)

Vienna, April 2021

Abstract

The Colles' fracture is the most common fracture and occurs proximal to the radiocarpal joint, also referred to as the Colles' fracture region. Treatment involves a distal radius implant and thus the stress distribution in the subchondral region is crucial for the structural integrity of the implant system. When modeling such an implant system using a finite element model, the question arises what level of detail regarding the boundary conditions (BCs) must be set to achieve a realistic representation of the stresses in the subchondral and Colles' fracture region. This thesis aims to address this question by comparing a model representing close to physiological BCs (referred to as a reference model) with models with simplified BCs.

A computed tomography scan was used to establish the finite element model of the reference model with contact interaction between the carpal bones and the cartilage of the radius. A parameter sensitivity study was performed and the response of the reference model to increased loads in terms of its linearity was investigated. Models with simplified BCs, involving an embedded model (EM) as well as a model with directly bonded carpal bones (BM), were compared to the reference model quantitatively in terms of the element wise normalized root mean square error of the effective stress as well as qualitatively using contour plots.

An increased stress concentration in the trabecular subchondral region with an uneven load distribution between the lunate and scaphoid was observed in the reference model due to the contact interaction between the carpal bones and the cartilage.

The qualitative comparison between models with simplified BCs and the reference model showed that the more complex the applied BCs, the stronger pronounced the stress concentrations in the subchondral trabecular region. If statically equivalent loads were applied, stresses in the cortex were represented similarly compared to the reference model for both simplified models (EM and BM), while stresses in the subchondral and Colles' fracture region of the trabecular region were underestimated. It was concluded that if correct reaction forces and moments are known and the region of interest lies within the Colles' fracture region, a large simplification of BCs can be utilized. If the stress distribution in the subchondral region is of interest, the application of statically equivalent loads and load transmission through carpal bones do not represent stress peaks sufficiently compared to a contact model and an error is unavoidable.

Kurzfassung

Die Colles-Fraktur ist die häufigste Fraktur im Menschen und entsteht proximal des Radiokarpalgelenks (auch Colles-Frakturbereich genannt). Die Behandlung einer solchen Fraktur beinhaltet das Setzten eines distalen Radiusimplantats im subchondralen Knochenbereich. Somit ist die Spannungsverteilung in diesem Bereich entscheidend für die strukturelle Integrität des Implantatsystems. Es stellt sich daher die Frage, wie detailliert die Randbedingungen in einem Finite Elemente Modell gesetzt werden müssen, um eine realistische Darstellung der Spannungen im subchondralen und Colles-Frakturbereich zu erreichen. Zur Beantwortung dieser Frage wurde sowohl ein eingebettetes Modell als auch ein Modell mit direkt verbunden Handwurzelknochen mit einem Modell mit nahezu physiologische Randbedingungen mit Kontakt (Referenzmodell) quantitativ, als auch qualitativ verglichen. Zusätzlich wurde eine Parametersensitivitätsstudie durchgeführt und die Reaktion des Referenzmodells auf erhöhte Belastungen hinsichtlich seiner Linearität untersucht.

Es wurde eine erhöhte Spannungskonzentration im trabekulären subchondralen Bereich mit einer ungleichmäßigen Lastverteilung zwischen Lunatum und Scaphoid aufgrund des Kontakts zwischen den Handwurzelknochen und dem Knorpel beobachtet.

Der qualitative Vergleich der Modelle zeigte, dass die Spannungskonzentrationen im subchondralen trabekulären Bereich umso stärker ausgeprägt waren, je komplexer die aufgebrachten Randbedingungen waren. Wurden statisch äquivalente Lasten aufgebracht, so wurden in der Kortex die Spannungen im Vergleich zum Referenzmodell für beide vereinfachten Modelle ähnlich dargestellt, während die Spannungen im subchondralen und Colles-Frakturbereich des trabekulären Bereichs unterschätzt wurden. Der Vergleich zeigte, dass die Art der Anwendung wesentlich für die Wahl des richtigen Modellansatzes ist.

Falls Reaktionskräfte und -momente bekannt sind und die Spannungsverteilungen im Colles-Frakturbereich gefragt sind, ist eine starke Vereinfachung der Randbedingungen ohne großen Fehler möglich. Ist andernfalls die Spannungsverteilung im subchondralen Bereich von Interesse, reicht das Aufbringen von statisch äquivalenten Lasten und die Lasteinleitung über die Handwurzelknochen jedoch nicht aus, um Spannungsspitzen im Vergleich zu einem Kontaktmodell ausreichend genau abzubilden, ohne einen erheblichen Fehler zu begehen.

Acknowledgements

I would like to thank my thesis supervisor Prof. Dieter Pahr who supported me with his great experience and expertise whenever needed and whose advice was greatly appreciated during the whole thesis work.

I would also like to thank my second supervisor Dr. Alexander Synek who guided me through the process of this thesis and supported me with valuable feedback with an eye for detail.

I also want to say thank you to my family and friends for their constant support throughout my whole education.

Affidavit

I declare in lieu of oath, that I wrote this thesis and performed the associated research myself, using only literature cited in this volume. If text passages from sources are used literally, they are marked as such. I confirm that this work is original and has not been submitted elsewhere for any examination, nor is it currently under consideration for a thesis elsewhere. I acknowledge that the submitted work will be checked electronically-technically using suitable and state-of-the-art means (plagiarism detection software). On the one hand, this ensures that the submitted work was prepared according to the high-quality standards within the applicable rules to ensure good scientific practice "Code of Conduct" at the TU Wien. On the other hand, a comparison with other student theses avoids violations of my personal copyright.

Vienna, April 2021 _____

Contents

List of Symbols

$\underline{\boldsymbol{F}}$	nodal force vector
$\underline{\boldsymbol{U}}$	nodal displacement vector
$\underline{\underline{K}}$	element stiffness matrix
m	mass
u	displacement
k	spring stiffness
ε	penalty stiffness
λ	Lagrange multiplier
$\underline{\underline{\sigma}}$	stress tensor
$\underline{\underline{\varepsilon}}$	strain tensor
U	strain energy density
E	Young's modulus
ν	Poisson's ratio
C_{10}	material parameter of the neo-Hookean material
D_1	material parameter of the neo-Hookean material
G	bulk modulus
K	shear modulus
F_i	force vector component
u_i	displacement vector component
ΔT_{max}	maximum increment size
$\Delta T_{\text{initial}}$	initial increment size
ΔT_{min}	minimum increment size
$r_{x,y,z}$	rotation in direction x,y,z
p_0	threshold at which the contact pressure was assumed zero
$\bar{\sigma}$	effective stress
$\bar{\sigma}_{\text{norm}}$	normalized effective stress
$\bar{\sigma}_{\text{max}}$	maximum effective stress
β	slope of the line of the best fit in linear regression model
ϵ	intercept of the line of the best fit in linear regression
R^2	squared Pearson's correlation coefficient
P_{contact}	contact pressure
P_{peak}	peak contact pressure
P_{mean}	mean contact pressure
A_{contact}	contact area
NRMSE	normalized root mean square
$\text{NRMSE}_{\text{Slice, max}}$	maximum normalized root mean square of all slices
$\text{NRMSE}_{\text{Region}}$	normalized root mean square of entire subchondral or Colles' fracture region

List of Acronyms

BC	boundary condition
BM	bonded model
Brep	boundary representation
CAD	computer aided design
CT	computed tomography
DoF	degree of freedom
DRF	distal radius fracture
EM	embedded model
FE	finite element
FEM	finite element method
NRMSE	normalized root mean square error
OBJ	wavefront object
RCJ	radiocarpal joint
RMSE	root mean square error
STEP	standard for the exchange of product data
STL	stereolithography

1 Introduction

1.1 Motivation

The distal radius fracture (DRF) is the most common fracture and occurs due to a fall on the outstretched hand [1]. The fracture site usually lies in between 2 to 3cm proximal from the radiocarpal joint (RCJ) [2]. Treatment of this fracture typically involves a distal radius implant, which is a locking plate fixed with screws onto the bone in close proximity to the articular surface [3]. These locking plate implants rely on the fixation in the region above the fracture site, which is referred to as the subchondral region of the bone [4]. Thus, the stress distribution in the subchondral region is crucial for the structural integrity of the implant system, which must withstand loads from everyday activities.

Finite element (FE) models have been heavily used to assess mechanical performance of the distal radius, with and without implant systems. There have been different approaches in modeling, which have led to a variety of models. To facilitate the calculations, assumptions of boundary conditions (BCs) are often simplified. On the one hand, studies involving experimental validation usually simulate a simplified uniaxial compression test with load application through embedding materials [5]. On the other hand, there are models which incorporate the carpal bones, but simplify contact interaction within the RCJ [6]. These simplifications of BC are based on the assumption that stress distribution differences will decrease quickly with increasing distance from the point of load application, if statically equivalent loads are applied (known as Saint-Venant's principle). However, bone is a complex material with irregular shape and the stresses of interest are fairly close to the point of load introduction (in this case the articular surface). Therefore, the predicted bone stresses and strains might not correctly represent those of physiologically loaded bones [7] and it is yet unknown what the effects of these simplifications on the stress distribution in the subchondral region of the radius are.

There have already been studies performed in terms of the comparison between simplified and more physiological BCs [6, 8]. Edwards and Troy [6] used a previously validated FE model [9] to predict DRF strength under BCs simulating a simplified loading of the radius and with physiological joint loading. They found that predicted fracture strength was highly correlated between both loading configurations, but physiological loading was

characterized by increased stress and strain concentrations. Albeit, they used a simplified contact interaction model in which the carpal bones were not free to move [6].
Johnson and Troy [8] compared load sharing within the cortical-trabecular compartments between experimental BCs and physiological BCs using a previously validated multiscale approach [10]. Cortical and trabecular loads from the experimental BCs simulations were strongly correlated to the physiological BCs simulations [8]. Nevertheless, only a 9mm section of bone was analyzed, leaving out the subchondral region of the bone [8].
Therefore, it is still unknown how the stress distribution in the subchondral region of the bone is affected if physiological BCs are used compared to simplified ones. The question arises what level of detail regarding the BCs must be set to achieve a realistic representation of the stresses in the subchondral and Colles' fracture region. Furthermore, it is of interest to quantify if the differences in these regions of interest are resulting from simplifications of BCs. In order to address the issue, the stress distribution obtained with simplified BCs should be compared with those obtained from more realistic BCs. Hence, this thesis aims to address this question by comparing a model representing close to physiological BCs with contact interaction (referred to as a reference model) with simplified models of different levels of complexity regarding their BCs.

1.2 Thesis Structure

Chapter 1 offers an overview and fundamental theoretical aspects of the finite element method (FEM), with a focus on a detailed description of contact interactions. In addition, the basics of bone mechanics, its composition, and an overview of the RCJ are presented. The end of the introductory chapter comprises the state of the art regarding RCJ modeling, leading to the research question and hypothesis of the thesis.
Chapter 2 describes the workflow for the establishment of the reference model, followed by a parameter sensitivity study of the reference model with regards to changes of its components and its response to increased loads. The methodology is concluded by detailed representations of the used models for comparison to answer the research question and hypothesis.
Chapter 3 summarizes the results of the reference model as well as the results of the parameter sensitivity and the analysis of the linearity of the subchondral bone stresses of the reference model. At the end, the comparisons between the reference model and the simplified models are drawn.
The discussion is given in chapter 4. The results of the reference model are discussed with regard to previously established models in literature. Furthermore, the sensitivity of the reference model to changes of its parameters is discussed and the limitations of the

study are given. The results of the comparison between the reference model and simplified models are discussed in the end.

1.3 Finite Element Method (FEM)

The following theoretical fundamentals are taken from the work of Bathe [11], if not specified differently. The FEM is a popular numerical method used to find solutions to continuum mechanics problems. In a first step, the problem is described by formulating the respective differential equations, which express the underlying physics of the problem. These differential equations have BCs, which describe the behavior of the problem at the boundary of the domain. In the FEM this domain is discretized into a finite set of elements. These elements are connected with each other via nodes and together form a mesh. The elements can be of various shapes such as lines (1D, e.g., beams), surfaces (2D, e.g., plates), or solids (3D, e.g., tetrahedral). Furthermore, the number of nodes involved in the formation of an element can vary among element types.
On the one hand, there are linear elements, for which the displacement of the mesh between the nodes changes linearly with the distance in between nodes. These elements therefore have linear shape functions.
Quadratic elements on the other hand have nonlinear shape functions and therefore the displacement between nodes is interpolated with a higher order polynomial. Hence, these elements have a larger number of nodes per element. A schematic representation of the different element types is given in Figure 1.1.

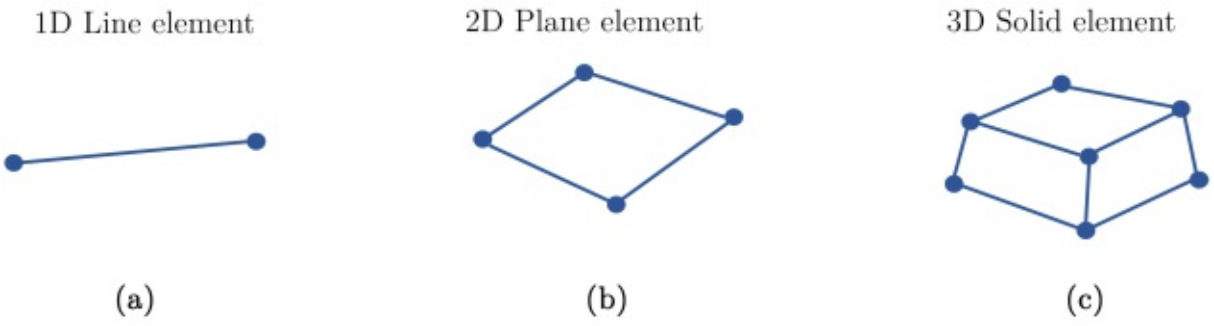

Figure 1.1: Representation of the different element types: (a) 1D line element, (b) 2D plane element and (c) 3D solid element (modified from: Yang, p.62, 67 [12]).

For each of the nodes of an element the nodal values of the field function are established as the parameters of the approximate solution. Therefore, a piecewise approximation for the displacement field of each element is established. In order to achieve this approximation, continuity requirements in the interior as well as at the boundaries of an element must be

satisfied. To represent this discretization of a domain in finite elements, a beam is given as an example (see Figure 1.2).

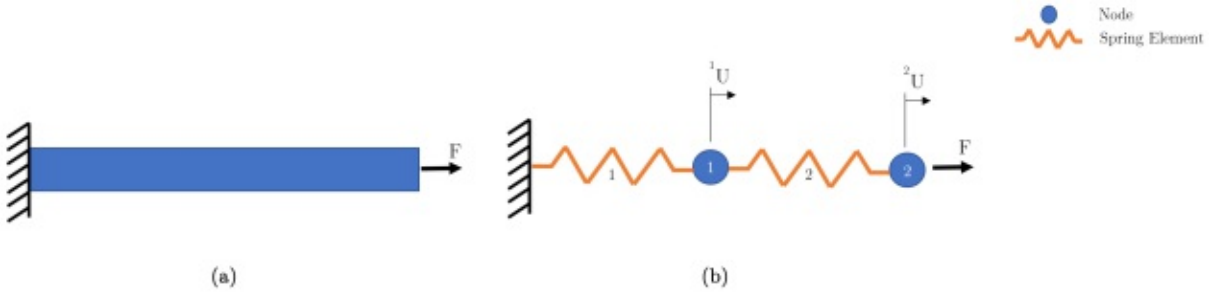

Figure 1.2: Schematic representation of the FEM. (a) A cantilever beam loaded at the right end; (b) discretization of the beam into finite elements (orange) and nodes (blue).

In this example, spring elements are connected to each other to discretize a beam with linear elastic material properties into finite elements. First, the nodal equilibrium equations are formulated taking into consideration the underlying BCs. Then, with the application of the displacement-strain relation and the use of the material law, the discrete governing equations of static equilibrium are formulated as

$$\underline{\underline{K}}\,\underline{\boldsymbol{U}} = \underline{\boldsymbol{F}} \tag{1.1}$$

where $\underline{\underline{K}}$ is the element stiffness matrix, $\underline{\boldsymbol{U}}$ is the nodal displacement vector and $\underline{\boldsymbol{F}}$ is the nodal force vector. $\underline{\underline{K}}$ is a symmetric matrix, which provides relation between the nodal displacements and the nodal forces and is calculated for each individual element. In order do achieve a response of the whole system, an assembly of the global stiffness matrix is performed. These governing equations are then solved using a matrix solving operation such as the Gauss elimination algorithm. Based on the calculated displacements, the stresses and strains can then be computed.
The advantages of the FEM are that complex geometries as well as loading scenarios can be solved. Disadvantages are that a general closed-form solution can not be produced and only an approximation of the result can be achieved [12].

1.3.1 Contact Modeling

The following subsections on contact modeling are based on the textbook of De Lorenzis et al. [13], if not specified differently. Contact is given if two or more parts are engaging in physical contact during a simulation. Unfortunately, the computational solution of contact problems can sometimes be quite difficult to achieve. This stems from the fact that, before contact is established, the contact area is unknown. Therefore, the

mathematical description of contact interaction results in a nonlinear boundary value problem. Essentially, contact interaction can been seen as a nonlinear spring between two parts. Its constitutive theory, and its essential components are contact constraint enforcement methods, discretization schemes, and solution algorithms.
Contact conditions in FE analyses are referred to as discontinuous constraints, for which forces can be transmitted from one part to another, only when the surfaces of these two parts are in contact [14]. Consequently, a force acting normal to the contacting bodies as well as shear forces may occur, if one surface slides along the other. Therefore, in a two-body contact problem kinematics are described separately in the normal and tangential directions. In such a two-body problem it is crucial to set one of the two contacting surfaces as the slave and the other one as the master surface [14]. This discretization between surfaces is necessary because slave nodes are constrained not to penetrate the master surface, while master nodes are permitted to penetrate the slave surface. As a guideline to set master and slave surfaces, the contacting surface with higher mesh density is preferably the slave surface. Furthermore, if the mesh densities are equal on the two surfaces, the surface which is thought to deform less, based on its material parameters, is suggested to be set as the master surface [14].
Since the contact areas are unknown before contact takes place, a contact detection must be performed. This involves two steps, first the global search for contact and second the setup of local kinematical relations which are necessary for the formulation of contact constraint enforcement methods. The global search for contact in the normal direction involves finding for each slave node the closest point of the master surface. Then the normal gap between these two points is calculated, which is usually performed utilizing a minimum distance function.

Pressure-Overclosure Relationships

Once the projection point of a given slave point on the master surface is known, constitutive laws for contact – also referred to as pressure-overclosure relationships - are applied. A pressure-overclosure relationship relates the applied pressure on the surface to the overclosure of the elements of these surfaces [15]. Again, these pressure-overclosure relationships are applied in the normal as well as the tangential direction.
Contacting surfaces can overlap at the beginning of an analysis, which is referred to as initial overclosure or penetration [16]. A distinction can be made between two types of initial overclosure: intended overclosure as an interference fit and unintended overclosure. Unintended overclosure can be caused either from poor computer aided design (CAD) modeling leading to overlapping of parts or due to discretization errors of curved surfaces without geometry corrections performed [16]. In this case the two touching geometries,

which have initially the same radius, are discretized with a different element size and therefore differ from their initial shape [16].

Since no actual penetration of one surface into the other can physically occur, the simplest formulation is a nonpenetration condition as a geometrical constraint. This pressure-overclosure relationship is often referred to as hard contact (see Figure 1.3a). The relationship between the normal contact pressure and the normal gap is given by the conditions that penetration is forbidden, only compressive contact normal stresses are present as well as the contact normal stress is reduced to zero when the gap is open and is negative when the gap is closed. Additionally, there is a soft pressure-overclosure relationship, for which the pressure-overclosure is given as an exponential function (see Figure 1.3b).

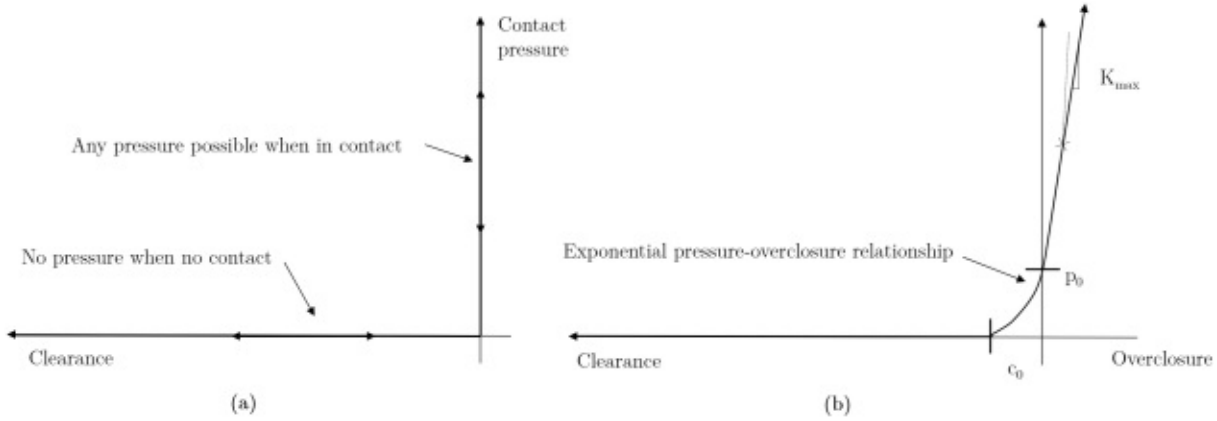

Figure 1.3: (a) Hard pressure-overclosure relationship; (b) Softened pressure-overclosure relationship (modified from Smith [15]).

Constraint Enforcement Methods

A contact problem can be seen as a classical mechanical problem with additional inequality constraints as a result of the contact conditions. These contact constraint enforcement methods determine how contact constraints are resolved during an analysis [15]. Some of the most commonly used methods are outlined in the following.

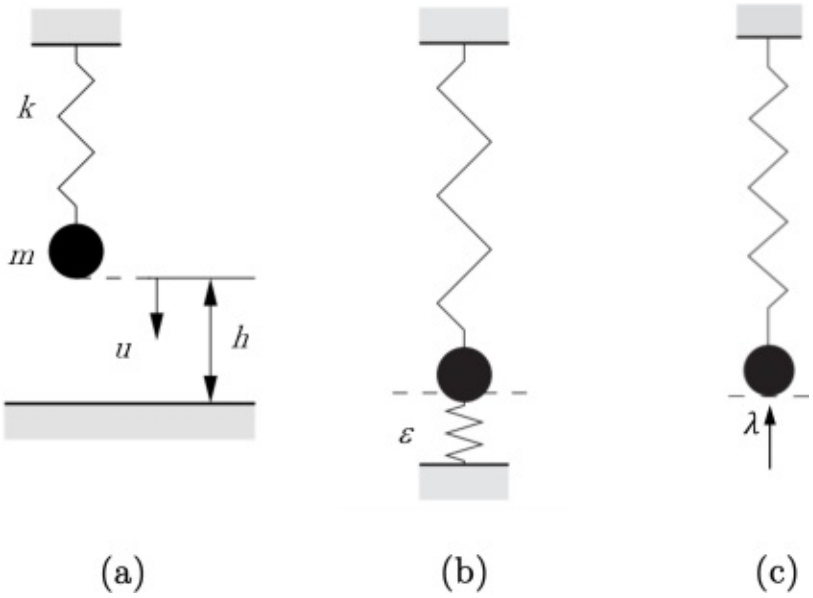

Figure 1.4: (a) Contact example with a mass m on a spring with stiffness k with a displacement u; (b) Penalty method with a nonlinear spring with the penalty stiffness ε once the mass is in contact with the surface (c) Contact example with the use of Lagrange multiplier λ (modified from: Wriggers, pp. 11, 16, 17 [17]).

Penalty Method

The penalty method adds a penalty term to the formulation of the governing inequality equation and is formulated for normal and tangential contacts. Therefore, the physical interpretation of the penalty method is given as the insertion of a nonlinear spring at the contact interface between the two bodies (see Figure 1.4b). Additionally, there is a special case of a linear spring, which is referred to as the linear penalty method. Despite some penetration occurring while choosing this method, there are advantages that the total number of unknowns is not changed, and the system equations generally behave well. However, the constraint equations can only be satisfied approximately.

Lagrange Multiplier Method

The method of Lagrange multipliers adds constraints to the inequality of the solids in contact. While on the one hand this method results in an exact enforcement of the contact constraints, it also introduces the unknown Lagrange multiplier vector, with normal and tangential components.

Augmented Lagrange Multiplier Method

In contact mechanics, the concept of augmented Lagrange multiplier is typically intended in two possible ways. The first and simplest option is a combination of the penalty and Lagrange multiplier methods, where, the Lagrange multipliers are not present as additional

unknowns, but approximated through an iterative procedure. The augmented Lagrange method uses essentially the same stiff approximation as the penalty method, with the addition of augmentation iterations for improved accuracy of the approximation. Therefore, it finds a converged solution using the penalty method in a first step. In a second step, the contact pressure is augmented, if penetration of a slave node exceeds the specified tolerance distance resulting in another series of iterations until convergence is reached. In a third step the contact pressure is continuously augmented until the solution is found resulting in an actual penetration smaller than the specified tolerance distance. The advantage of the augmented Lagrange method is that, even though additional iterations may be required, the resolution of the contact conditions is facilitated, and overconstraint issues are solved [15].

Contact Space Discretization

While the first main part of contact constraints is the contact enforcement method, the second one is the discretization of the contact space. The two bodies can either be discretized with conforming or nonconforming meshes at the contact boundary. Furthermore, it is of interest if small or large deformations are expected.
A distinction is made between different numerical methods for contact interaction. Node-to-node contact builds contact constraints between individual pairs of nodes and was introduced by Francavilla and Zienkiewicz [18]. Due to its rare use, it is not further discussed in this thesis. In the following the two more commonly used methods for contact space discretization - node-to-surface and surface-to-surface - are discussed.

Node-to-Surface

For node-to-surface interaction each node of the slave surface is assigned the closest point in normal direction on the master surface. The interaction is then discretized between the point on the master surface and the slave node [15] (see Figure 1.5a). During the contact condition, so called contact elements are established. Each contact element is comprised of a slave node and of the respective closest master surface. Nevertheless, this projection of the point can also be non-unique or not given at all.

Surface-to-Surface

Simo et al. [19] formulated the surface-to-surface contact interaction, for which contact is enforced on an integral over a region surrounding the slave nodes (see Figure 1.5b). In the surface-to-surface contact interaction the contact pressure is approximated over the contact interface [19]. The surfaces are treated as an assembly of contact segments [19]. Due to the assumptions of constant contact pressure on each contact segment, the contact constraint is enforced in an average sense on each contact segment [19]. Therefore, the

main difference compared to the node-to-surface interaction is that multiple constraints are generated at the surface per node, while the node-to-surface interaction only results in a single constraint in normal direction at the surface.

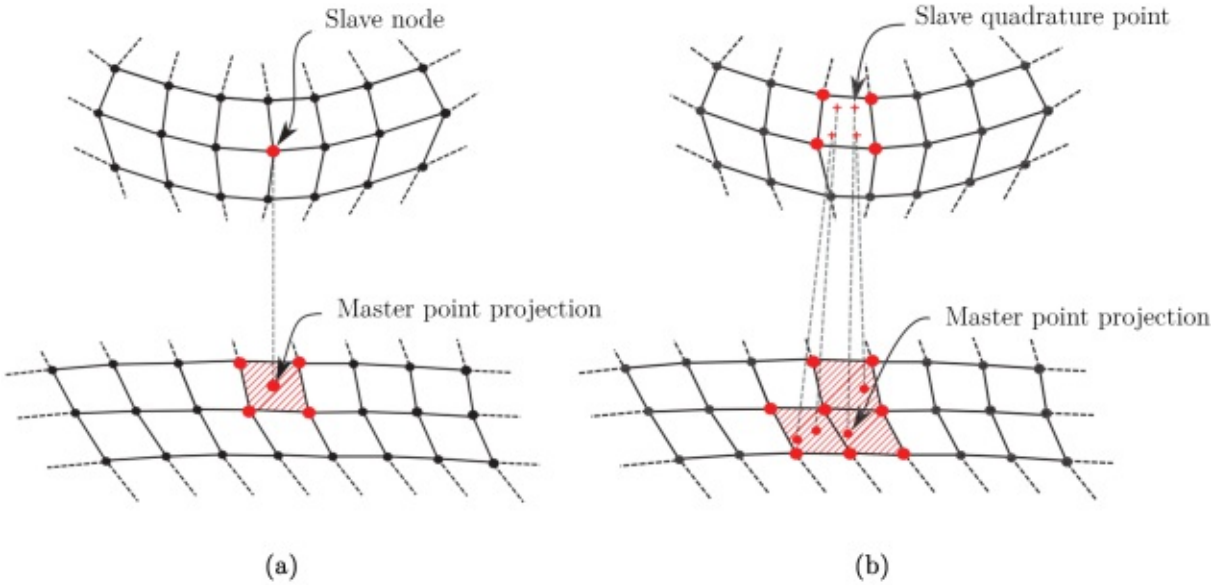

Figure 1.5: Schematic representation of the node-to-surface contact interaction algorithm (modified from: De Lorenzis et al., pp. 19, 22 [13]).

Additionally, there are also smoothing procedures, which generally improve the performance of the contact algorithms [13]. For these smoothing techniques, the continuity of the master surface is improved and therefore provides a unique definition of the normal and tangent vector fields [13]. The slave surface on the other hand is kept unchanged.

1.4 Basics of Bone Mechanics

Bone is the primary structural element that forms the skeletal system [20]. It is a living tissue, which provides not only shape but also kinematic links between different body parts [21]. Furthermore, it serves as the attachment site for muscles and hence is essential in human movement [20]. Due to its structural support for organs, it also protects them from external impacts [20]. In order to fulfill all its tasks while keeping its weight low, bone has a complex hierarchical structure (see Figure 1.6).

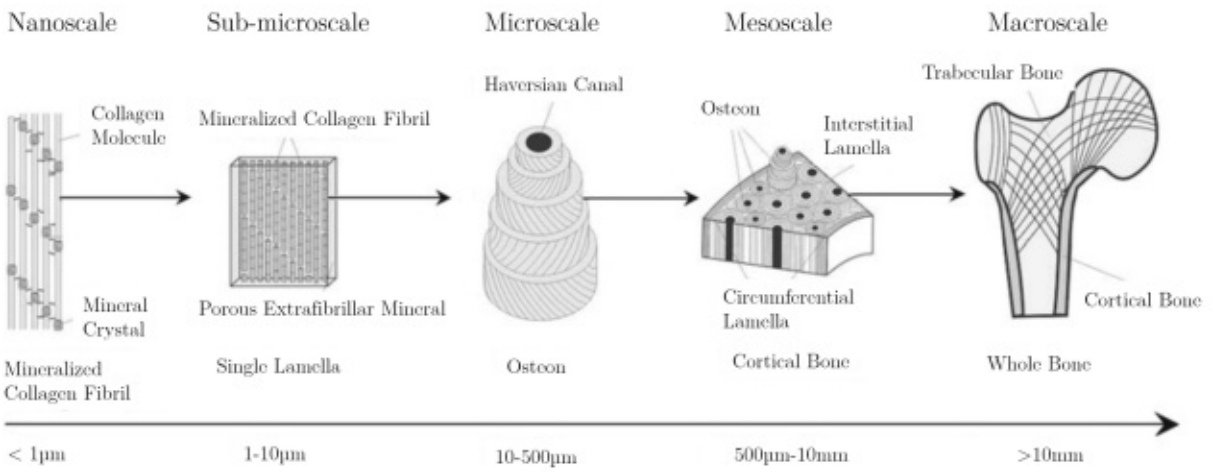

Figure 1.6: Hierarchical structure of bone (modified from Hamed et al., p. 23 [22]).

The following fundamentals on bone are based on the textbook of Ethier [23], if not stated differently. The whole bone at the macroscopical level can take several forms and sizes depending on its location in the human body. One of the mechanically most relevant types are long bones. Long bones are divided into different parts by the shape of their components. Both ends, called epiphyses, are covered with articular cartilage at the joints and are connected via the shaft. At the macroscopical scale, the whole bone is further subdivided into the cortical and trabecular bone.

Cortical and trabecular bone are primarily distinguished by their porosity. The trabecular region of a long bone is situated in the epiphysis and fills all space in irregular bones. It transfers loads from the joint faces via the mid shaft to the end of the bone reducing stress concentrations along the way.

Trabecular bone is organized by a network of 3D structures called trabeculae with an average size of roughly 200μm in healthy bone. Due to its porous composition, it shows inferior mechanical properties compared to cortical bone. Though, the high porosity helps to keep the weight of the entire bone low.

Cortical bone on the other hand, enhances the mechanical properties by acting as a shell around the porous trabecular bone. It surrounds trabecular bone and is thicker along the shaft than at the epiphyses of a long bone. Due to its lower porosity compared to trabecular bone, it provides strength and stiffness to the bone. Its tissue is arranged in lamellae of roughly 5μm thickness and the collagen fibers run parallel to each other within each layer. Depending on the location in the bone, the lamellae are arranged differently. For example, they are circumferentially arranged and parallel to each other near the outer and inner surfaces of bone. In between these two layers, the osteons form most of the cortical bone. Osteons are roughly 200μm in diameter and aligned with the long axis of

the bone. Nutrients are passed to the bone through a highly interconnected network of channels and canals also hosting cells inside the bone called osteocytes.
Cortical bone shows anisotropic properties due to the longitudinal alignment of osteons and the orientation of lamellae. Hence, it is sensitive to the orientation of loading. As a result, cortical bone shows larger stiffness and strength along the longitudinal axis than its transverse axis. Keeping in mind, that bone is usually loaded in compression, it seems obvious that it is stronger in compression than in tension. Therefore, cortical bone is often regarded as transversely isotropic (see Figure 1.7).

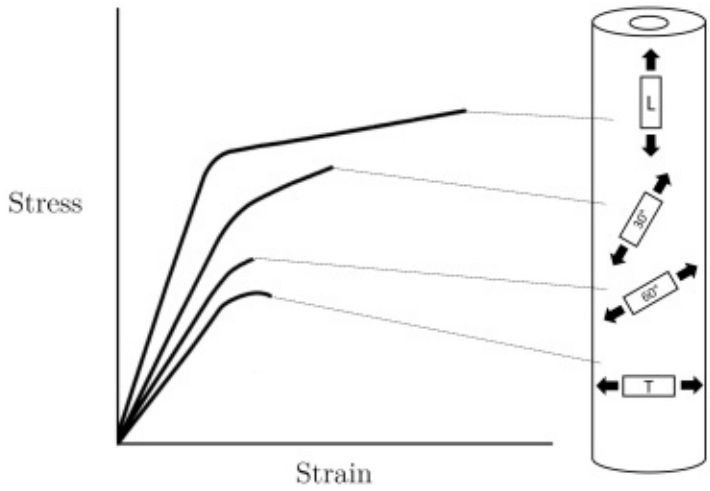

Figure 1.7: Transversely isotropic behavior of bone (modified from Smith, William and Hashemi, p. 939 [24]).

Trabecular bone is assumed to have about 20 to 30% lower stiffness than cortical bone [25]. This difference is believed to stem from the microstructural differences, in particular the lamellar and collagen organization and orientation [25].

1.5 Radiocarpal Joint (RCJ)

1.5.1 Anatomy

The human hand consists of a total of 27 individual bones [21]. Eight of these form the wrist together with the radius and ulna. These eight bones are called carpal bones and are arranged in two rows of four bones each as displayed in Figure 1.8a. While five carpals are connected distally to the metacarpal bones and form the mediocarpal joint, the scaphoid and lunate form together with the radius the RCJ as depicted in Figure 1.8b. Further proximal, there is the radioulnar joint formed between the radius and ulna. Additionally, the wrist can also be divided into three longitudinal columns based on the involved carpal bones - the scaphoid, lunate and triquetrum column. The scaphoid and lunate columns

are the main route for force transmission within the hand and therefore frequently affected in the event of injuries [21] (see section 1.5.2).

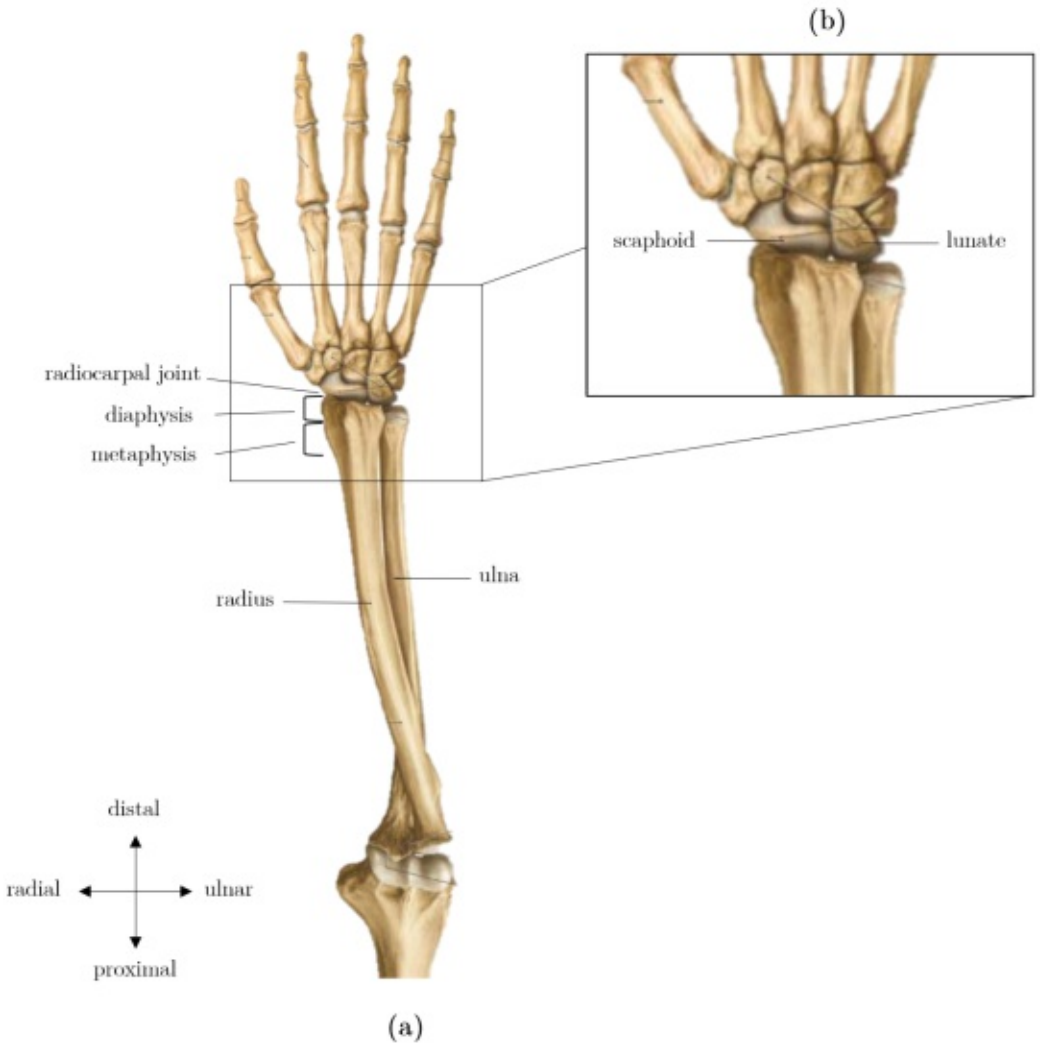

Figure 1.8: (a) Anatomical representation of the hand (dorsal view) and (b) detail of the RCJ (modified from Schünke et al., p. 247 [21]).

The RCJ is an ellipsoid joint which allows for palmar flexion and dorsal extension as well as radial and ulnar abduction. Articulation of the RCJ is facilitated through cartilage at the articulating surfaces of the radius as well as at the carpal bones [20].

1.5.2 Distal Radius Fracture and Treatment

The DRF is the most common fracture in the human body with a share of 20 to 25% of all fractures [1]. Eighty percent of women over 50 years of age are affected due to the presence of postmenopausal osteoporosis [1]. Depending on the position of the wrist in relation to the distal radius at the time of a fall, extension fractures - also known as Colles' fractures - occur in 90% and flexion fractures - also known as Smith fractures - only in

10% of all cases [21]. Therefore, the DRF will be used synonymously with Colles' fracture in this work.

A further distinction is made between extra-articular and intra-articular fractures in DRFs [21]. While the location of extra-articular DRFs has usually been reported to be in the range between 2 to 3cm proximally from the RCJ articular surface [21], no actual consensus exists on the fracture location of DRFs. Therefore, Baumbach et al. [2] investigated the correct location of DRFs in a systematic evaluation and found, in comparison with literature, that the fracture line of DRFs occurs further distal, around 11.7 ± 3.9mm proximal to the fossae of the radial head.

Treatment of DRFs is either surgical or nonsurgical. Nonsurgical treatment for DRFs is usually performed for minimally displaced fractures and involves immobilization through a placement of the limb in a plaster splint [26]. Surgical treatment involves the external or internal fixation of the bone. Numerous different fixations devices exist such as volar or dorsal locking plates or bridge plates [26]. Among these, the volar locking plate is the most commonly used [27] and shows improved radiographic as well as clinical outcomes [26]. The volar locking plate is fixed with screws onto the bone [3] and relies on the fixation in the region above the fracture site and in close proximity to the articular surface, which is referred to as the subchondral region of the bone [4]. Thus, the stress distribution in the subchondral region is crucial for the structural integrity of the implant system, which must withstand loads from everyday activities. A representation of the subchondral region and the Colles' fracture region is given in Figure 1.9.

Surgical treatment of the DRFs shows improved results in terms of anatomic reduction and grip strength compared to nonsurgical treatment [4]. Furthermore, surgical treatment has shown to result in fewer complications, such as malunion of the fracture sites [28].

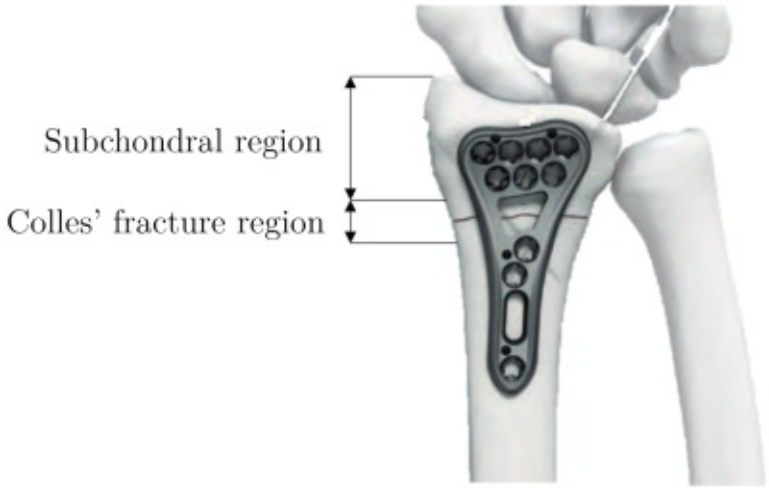

Figure 1.9: Representation of Colles' fracture and distal radius implant plate (volar locking plate) with a schematic distinction between subchondral and Colles' fracture region (modified from: Implants Inc. [29]).

1.6 Boundary Conditions in RCJ FE Models

In addition to clinical and experimental studies in the research of DRF treatments also FE models are frequently utilized to assess the mechanical performance. These FE models are used to simulate biomechanical experiments and give a better insight into the bone's and implant's responses to mechanical loading. Models employed for the assessment of volar and dorsal locking plates as well as fracture strength involve different approaches in modeling and have led to a variety of models. While similar in their general approach of modeling the RCJ, these FE models use different BCs depending on their use in research or clinical application.

When comparing different BCs with another, the Saint-Venant's principle, established by Adhémar Jean Claude Barré de Saint-Venant in 1855, comes to mind. It states that:

"If the forces acting on a small portion of the surface of an elastic body are replaced by another statically equivalent system of forces acting on the same portion of the surface, this redistribution of loading produces substantial changes in the stresses locally but has a negligible effect on the stresses at distances which are large in comparison with the linear dimensions of the surface on which the forces are changed." [30]

Thus, this principle allows to replace complex BCs with ones of less complexity, given that the stresses of relevance are remote from the point of load introduction. Nevertheless, the situation is not straightforward in bone.

Bone is a complex material with irregular geometry [31]. Long bones, such as the radius, are made of cortical and trabecular bone, which hold unique mechanical behaviors as well as complex interactions between the two regions [32, 33]. The trabecular region plays a key role in the transfer of the loads form the joint to the cortex [34].

Therefore, it remains unknown at which distance from the articular surface the stresses, which are caused by complex but statically equivalent loads, will decay. Even though, stresses decay at some point, due to the Saint-Venant principle, it is yet unknown, how far into the bone stresses reach before they have fully decayed. For instance, the much stiffer cortex might carry most of the applied load and therefore the subchondral trabecular region might not be affected at all. Hence, it is of interest to understand how the subchondral region and the Colles' fracture region are affected by differently applied BCs while statically equivalent loads are applied, when modeling the RCJ.

1.6.1 Literature Review

Due to different applications of FE models in the research and treatment of DRFs, various approaches regarding the modeling procedures as well as the employed BCs have emerged. In the following, the differences in terms of BCs applied in a selection of models are

presented. This selection is intended to picture an excerpt of the differences in BCs in FE modeling and is not a complete review of the numerous other studies already performed. In the simplest models, a force is applied onto the center of the articular surface to simulate the pressure transferred through the carpal bones [35–37] (see Figure 1.10a).

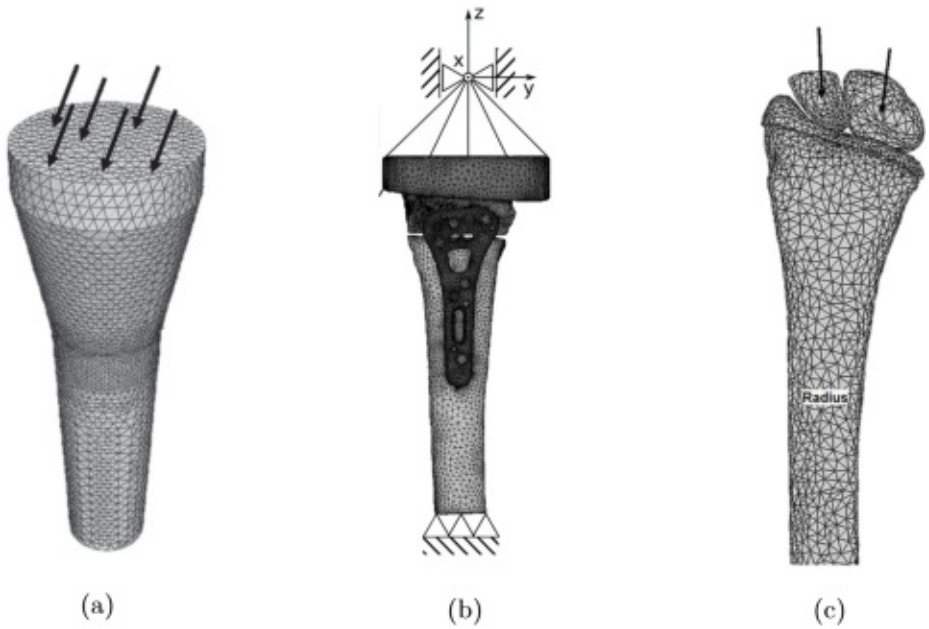

Figure 1.10: Representation of different modelling approaches of the RCJ loading.
(a) Uniform application of force onto the articular surface by Ural [37];
(b) uniaxial compression test loading with embedding by Synek et al. [38];
(c) physiological loading through modeling of the carpal bones and contact or tied interaction by Johnson and Troy [10].

Furthermore, there are models, which simulate a simplified uniaxial compression test between two embeddings in which the proximal surface of the bone section is fixed and a uniform axial displacement (or load) is applied to the distal surface [38] (see Figure 1.10b). In order to correctly represent the physiological interaction between the carpal bones and the radius, in a few models the carpal bones are included but tied to the radius (i.e., no contact interaction) (see Figure 1.10c). Pistoia et al. [39] for example, tied two cartilage layers of carpal bones and radius together to mimic physiological loading.
While an abundance of studies used rather simplified BCs, the question of how these simplifications affect the model has emerged. Hence, there have already been attempts made to compare physiological and experimental loading conditions with each other with regards to the RCJ.
Edwards and Troy [6] for example, used a previously validated FE model [9] to predict DRF strength under BCs simulating a simplified loading of the radius and with physiological joint loading. They found that predicted fracture strength was highly correlated between both loading configurations [6]. However, physiological loading was characterized by increased

stress and strain concentrations and decreased cortical shell load carriage, resulting in fracture strength values less than half those predicted for the simplified loading condition. This leads to the assumptions that there are differences in terms of the stress distribution in close proximity to the articular surface if physiological BCs are used compared to simplified ones. Nevertheless, the authors used a simplified contact model in which the carpal bones were not free to slide.
Another study by Johnson and Troy [8] compared load sharing within the cortical-trabecular compartments between experimental BCs and physiological BCs using a previously validated multiscale approach [10]. The outcomes showed that cortical and trabecular loads from the experimental BCs simulations were strongly correlated to the physiological BCs simulations. However, a 30% difference in cortical loads distally, and a 53% difference in trabecular loads proximally was observed with embedded BCs. Hence, the authors concluded that that experimental BCs simulations alter cortical-trabecular load sharing compared to physiological BCs simulations [8]. Although, in this study the authors modeled contact interaction between the radius and the cartilage, only a 9mm section of bone was analyzed, leaving out the subchondral region of the bone entirely.
Therefore, it is still unknown what the effects of the application of simplified BCs compared to physiological ones with contact interaction on the subchondral region of the radius are. Regarding the Colles' fracture region, there are studies that successfully replicated Colles' fractures by using an embedding experimental setup [40]. Hence, it is assumed, that the stress differences might already have decayed at this distance from the articular surface or are only present to some minor extent.
Based on these facts and the assumptions given above, the research question and hypothesis are formulated and given in the following section.

1.7 Research Question and Hypothesis

The goals of this thesis were as following: first, a workflow is established to create a FE model from computed tomography (CT) data suitable for contact interaction. Based on this workflow a reference model acting as the gold standard is created for further comparisons with simplified models. Second, the model's sensitivity is investigated by varying its parameters. Third, the reference model is compared to models of different levels of simplifications regarding their BCs.
Based on the fact that it is still unknown what the effects of the application of simplified BCs compared to physiological ones with contact interaction on the subchondral region of the radius are, the research question was formulated as: what level of detail regarding the BCs at the RCJ must be used to achieve a realistic representation of stresses in the subchondral and Colles' fracture region?

Therefore, the hypothesis of this thesis was formulated as: simplifications of BCs of RCJ FE models lead to significant changes of bone stresses in the subchondral region, but minor differences in the Colles' fracture region.

2 Methodology

This chapter is divided into four different sections. First, the workflow to create the reference model and the methodology are described in detail (see section 2.1). Then, the methodology regarding the parameter sensitivity study is portrayed and the different model alterations are investigated (see section 2.2). In the third section, the used methodology to investigate the linearity of the subchondral bone stresses in the reference model is described (see section 2.3). Last, the different simplifications of BCs are depicted and each simplified model is displayed in detail (see section 2.4).

2.1 Reference Model

The reference model was built based on a CT scan and parameters were taken from literature. The workflow of the modeling procedure is shown in Figure 2.1. The following subsections explain the modeling workflow in detail.

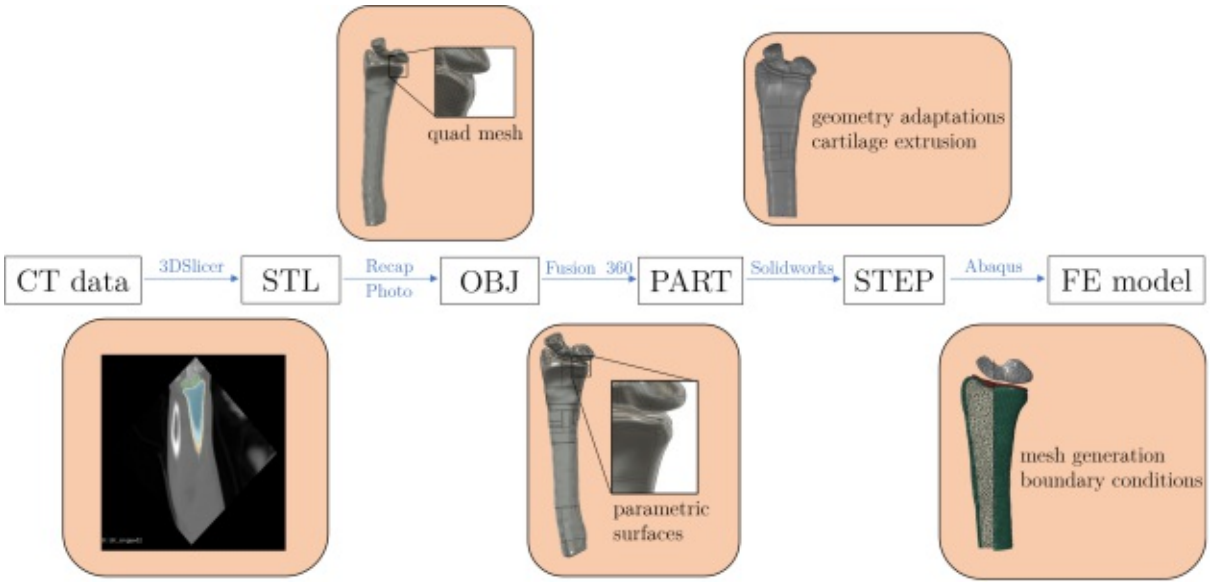

Figure 2.1: Flow chart representation of the workflow to create the reference model from CT data up to the final FE model. The used software of each step is given in blue font.

2.1.1 Image Data and Processing

A representative (53 years, 1.69m, 79.5kg) full body CT scan with an anisotropic voxel size of 1.27x1.27x0.25mm from the Swiss Institute for Computer Assisted Surgery Medical Image Repository (https://www.smir.ch) [41] was taken as the image source.
The open-source medical image processing software 3DSlicer (https://www.slicer.org/) [42] was used for image segmentation and image processing. The images were first cropped manually to only include the forearm and hand to cut computational cost for further processing. The CT scan showing the radius and carpal bones is depicted in Figure 2.2a. The images were then isotropically resized to a voxel size of 0.25x0.25x0.25mm. A threshold-based segmentation was used to segment the cortical bone structure from the surrounding tissue. Since the voxel size did not lead to the desired segmentation results, manual segmentation was additionally performed. Smaller islands of which were not considered bone were removed using a filter, for which a unique label value for each connected region was created. As a result, the connected regions were defined as groups of pixels which touched each other but are surrounded by zero valued voxels [43]. The carpal bones, the cortex and the trabecular region were segmented as individual segments with the use of the "wrap solidify" extension. The final segmentation is displayed in Figure 2.2b. The masked image was smoothed using first a median filter with a kernel size of 3mm and second a joint smoothing filter [44] with a smoothing factor of 0.55, where multiple segments where smoothed at once, preserving interfaces between them [45]. A rendered view (isosurfaces) of the model is displayed in Figure 2.2c.

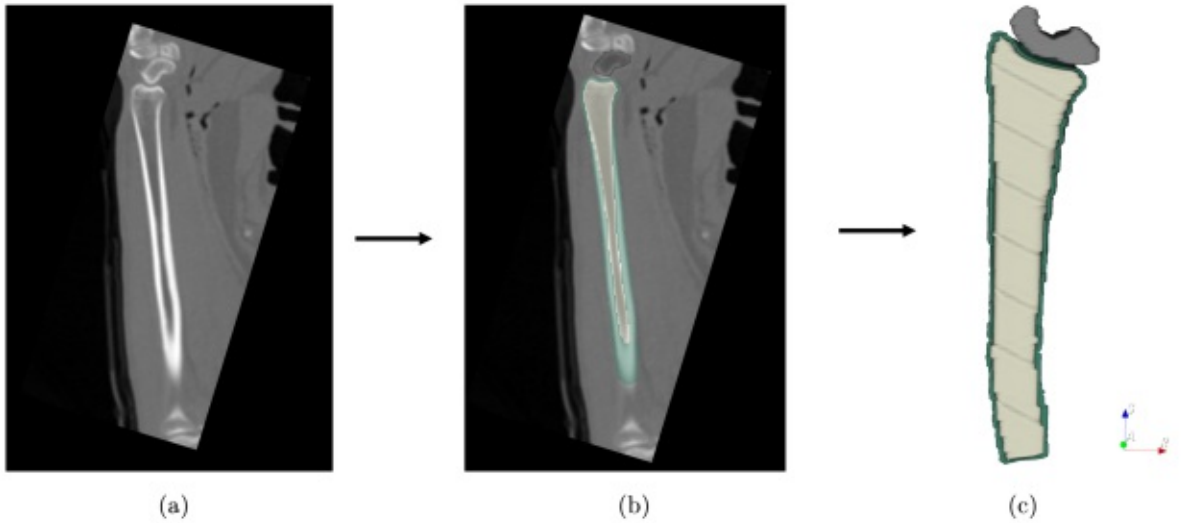

Figure 2.2: CT scan showing the radius and carpal bones (a); segmentation of the trabecular (beige), cortex (green) and carpal bones (grey) (b); rendered view (isosurfaces) of the model.

2.1.2 Geometry Adaptations

All three segments were exported as a stereolithography (STL) file. The STL file was further imported into Meshmixer (Autodesk, Inc., San Rafael, CA, USA) and remaining stair artifacts were removed as depicted in Figures 2.3a and b using the "RobustSmooth" option in Meshmixer [46].
In a next step, the resulting STL file was imported into Autodesk Recap Photo (Autodesk, Inc., San Rafael, CA, USA) and converted into a quad mesh wavefront object (OBJ) file. The OBJ file was then imported into Autodesk Fusion 360 (Autodesk, Inc., San Rafael, CA, USA) and first converted from a quad mesh into a T-spline geometry and subsequently into a boundary representation (Brep) geometry as shown in Figures 2.3c and d. This Brep geometry consisted of parametric surfaces, which allowed for further geometrical adaptations.
The resulting Brep geometry was then exported as a standard for the exchange of product data (STEP) file and Solidworks (Dassault Systèmes ,Vélizy-Villacoublay, France) was used to apply geometrical adaptations to the CAD model necessary to create the final model.

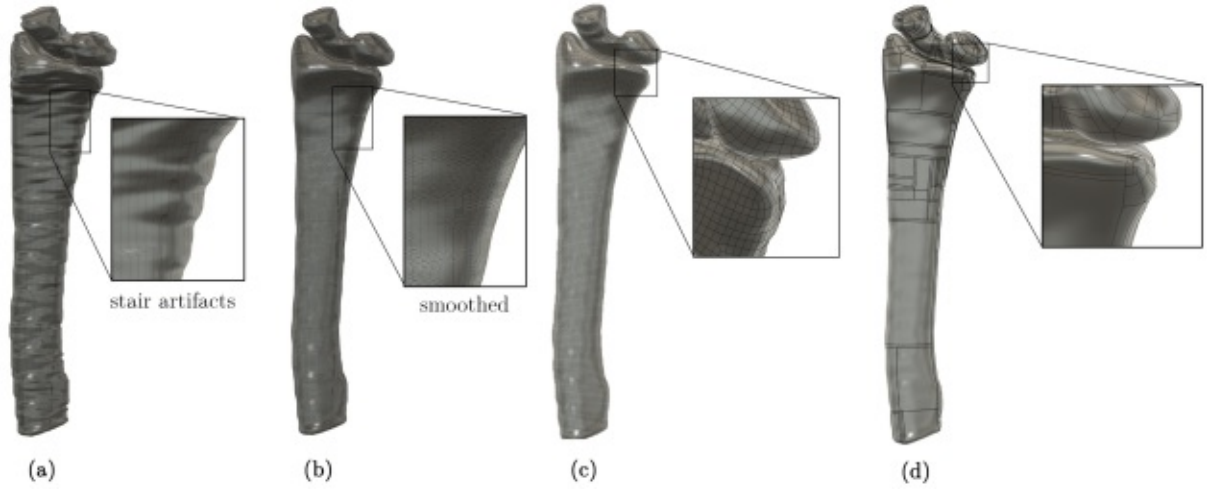

Figure 2.3: Staircase artifacts before (a) and after smoothing (b); (c) quad mesh OBJ file; (d) Brep file with parametric surfaces.

In Solidworks the coordinate system of the radius was set based on the recommendations of the international society of biomechanics [47]. The procedure is explained in the following and the resulting coordinate system is displayed in Figure 2.4.
Given the assumption that the forearm is initially in the standard anatomical position, with the palm oriented forward (anterior), and the thumb arranged laterally, while the dorsum of the hand and forearm face posteriorly. The origin was placed at the proximal end of the radius on a line between the ridge between the radioscaphoid fossa and the radiolunate fossa and the proximal radius at the level of the depression in the proximal

radial head [47]. In the transverse plane the origin was located at the approximate center of the bone along its principal axis of inertia. The z-axis was set as the line parallel to the shaft of the radius from the origin to intersect with the ridge of bone between the radioscaphoid fossa and the radiolunate fossa [47]. The x-axis was positioned perpendicular to the z-axis. The y-axis was set as the line perpendicular to the z- and x-axes. The bone was cut to have a length of 100mm from the tip of the radial styloid process.

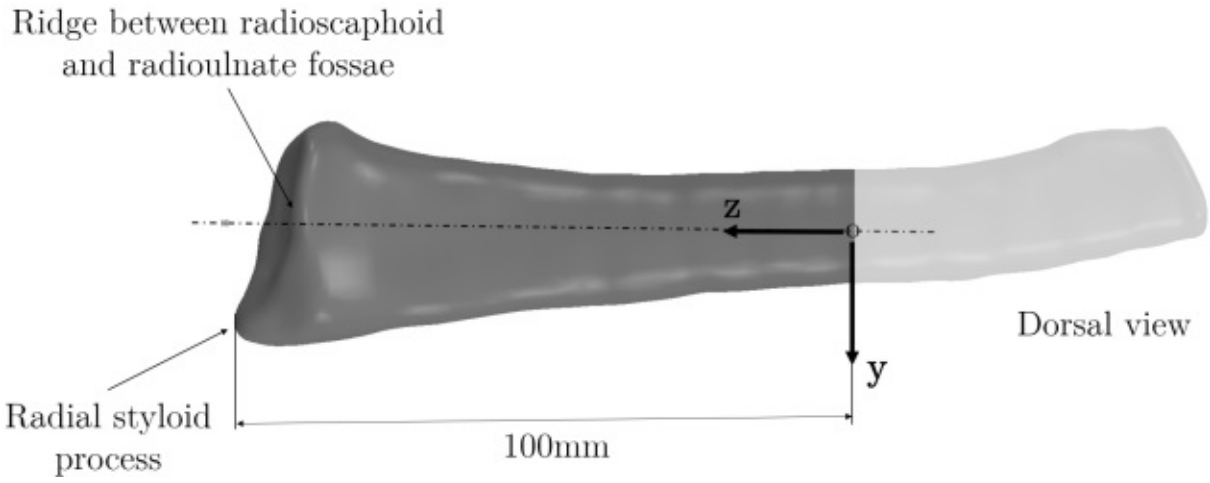

Figure 2.4: Schematic representation of the placement of the coordinate system and the applied cut to the radius.

The articular cartilage was created on the distal end of the radius by extruding the surface geometry in the local normal direction. The cartilage thickness for the reference model was chosen based on the work of Pollock et al. [48], where the authors found a cartilage thickness of 1mm to be an acceptable thickness for modeling. This thickness of 1mm was in agreement with other studies modeling the RCJ previously mentioned in section 1.6. The geometry of the carpal bones, the cortex, trabecular region and cartilage where then exported as a STEP file. The STEP file was then imported into Abaqus 2020 (Dassault Systèmes, Vélizy-Villacoublay, France) where the FE model was established as described in the following sections.

2.1.3 Mesh

Each part of the model was imported as an individual part into Abaqus. The parts were then assembled and the cortex and trabecular regions were merged as an independent instance to ensure consistent meshing of the two parts. Cortex and trabecular regions as well as cartilage were meshed using C3D10 quadratic tetrahedral elements, while the carpal bones were meshed using R3D4 shell elements. Quadratic tetrahedral elements were chosen based on the findings of Maas et al. [49], who showed that they offer an excellent alternative to hexahedral elements especially for simulation of articular contact (in this

case the hip joint). The cartilage was modeled as a single layer of elements based on the findings of Varga et al. [50]. There was no local mesh refinement performed, since in the contact region of carpal bones and cartilage, the mesh of the cartilage was already denser than the one of the carpal bones.

FE model accuracy depends on mesh size and is required to ensure that an accurate solution is achieved independent of mesh size [51]. A mesh is considered accurate enough if the result of a certain variable in the model does not continue to change with decreasing mesh size and hence converges with an increase in mesh density. Therefore, a mesh convergence study was performed for the reference model. The element size of the mesh of the model was decreased by almost half the size of the previous mesh. The successive change of mesh density was performed uniformly throughout the model for all different parts. The strain energy density (U) of the model was chosen as the variable of interest of the mesh convergence study. For linear isotropic materials undergoing small strains, U is defined as

$$U = \frac{1}{2}\sum_{i=1}^{3}\sum_{j=1}^{3}\sigma_{ij}\varepsilon_{ij}, \tag{2.1}$$

where σ_{ij} and ε_{ij} are the respective stress and strain components of the stress tensor $\underline{\underline{\sigma}}$ and strain tensor $\underline{\underline{\varepsilon}}$. The mean strain energy density (U_{mean}) was considered as the parameter to quantify the change between the differently meshed models [52]. The used material parameters, BCs as well as interactions are described in the following sections of the methodology. A change of less than 2% in U_{mean} compared to the finer mesh was considered as a converged solution. The result of the mesh convergence study is presented in Figure 2.5. Based on the results of the mesh convergence study, the average element size was set to 1.4mm which resulted in 81202 elements for the entire model.

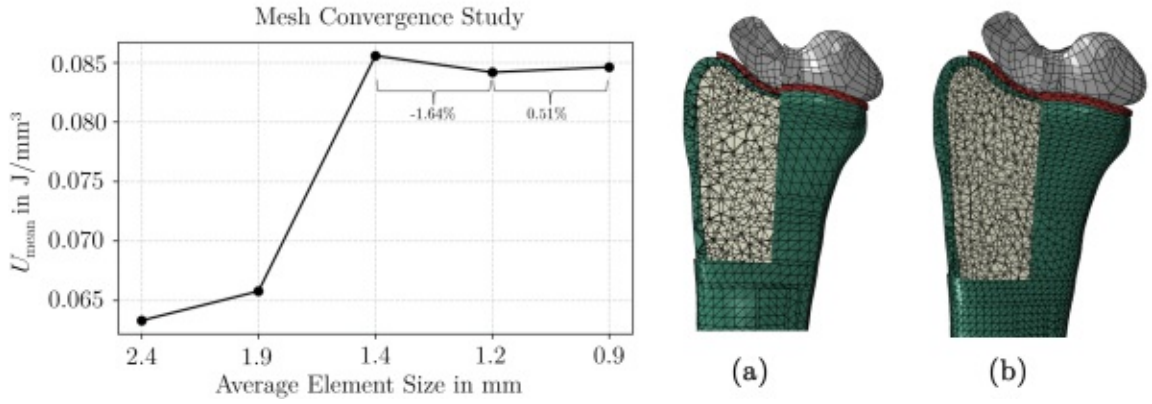

Figure 2.5: Mean strain energy density (U_{mean}) in J/mm^3 within the models meshed with different element sizes. (a) Mesh of the model with an average element size of 2.4mm and (b) of the converged model with an average element size of 1.4mm.

2.1.4 Materials

The trabecular and cortex regions were assumed as isotropic homogeneous elastic materials with E=1.4GPa and E=17GPa, respectively and a Poisson's ratio of ν=0.3 [38]. The cartilage was set to be a hyperelastic nearly incompressible neo-Hookean material. The Young's modulus was set to E=10MPa based on the work of Edwards and Troy [6] and the Poisson's ratio was assumed as ν=0.45 based on a range of ν from 0.45 to 0.49 found in the literature [8, 53]. Since Abaqus requests the material parameters C_{10} and D_1 for the modeling of hyperelastic neo-Hookean material, the following was considered.
The shear modulus G and bulk modulus K are defined by the Abaqus Manual [15] as

$$G = 2C_{10}, \quad \textit{and} \quad K = \frac{2}{D_1}, \tag{2.2}$$

where C_{10} and D_1 are material parameters required by Abaqus for the definition of a neo-Hookean hyperelastic material. Rearranging terms and considering $G = \frac{E}{2(1+\nu)}$ and $K = \frac{E}{3(1-2\nu)}$ yields

$$C_{10} = \frac{G}{2} = \frac{E}{4(1+\nu)} \qquad \text{and} \qquad D_1 = \frac{2}{K} = \frac{6(1-2\nu)}{E}. \tag{2.3}$$

Based on the given values of E and ν from the above Equation (2.3) it resulted in C_{10} = 1.724MPa and D_1 = 0.060MPa^{-1}.

2.1.5 Boundary Conditions

The carpal bones were assumed as a single rigid body for the sake of simplicity. A reference point was set to control the rigid body motion along the z-axis at 1cm above the radial styloid process. The radius was constrained at the proximal end using an encastre and at the reference point for all degree of freedoms (DoFs) except the displacement in vertical z-direction.
The model was solved using a two-step approach. First, a vertical displacement (u_z) was applied to the reference point, such that the carpal bones were just in contact with the cartilage. This was ensured using a python script, which stopped the step once the vertical reaction force at the reference point exceeded a value of 5N. Then in a second step, a ramped quasi-static load of 250N was applied in vertical z-direction (F_z) to the reference point and the contact conditions were applied. A schematic representation of the two-step approach is given in Figure 2.6.
A force of 250N was chosen based on the assumption of a load present in the RCJ for maximum hand grip strength in the neutral joint position [54].

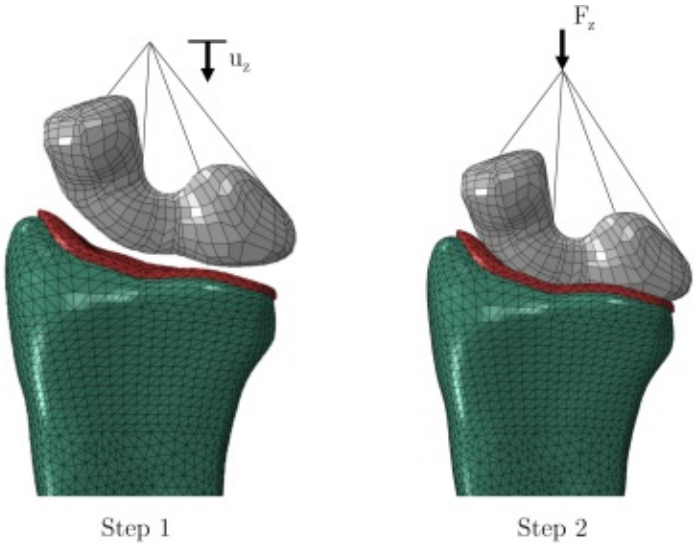

Figure 2.6: Two-step approach of applying BCs in the reference model. In step 1 a vertical displacement (u_z) was applied. In step 2, the model was loaded with a vertical force F_z=250N.

The geometric nonlinearity of the model was accounted for by the use of the nonlinear geometry parameter (NLGEOM) in Abaqus for both steps. The total step time for both steps was set to $T_{\text{total}} = 1$ with a maximum number of increments of 100, while the maximum increment size was $\Delta T_{\text{max}} = 1$. For the first step, the initial increment size was $\Delta T_{\text{initial}} = 0.25$ and the minimum increment size was $\Delta T_{\text{min}} = 0.125$. For the second step, in which the load was applied, $\Delta T_{\text{initial}}$ was set to 0.0001 and $\Delta T_{\text{min}} = 0.00005$. Unsymmetric matrix storage with the direct equation solver and full Newton solution technique were chosen for both steps. Calculations were performed on a 12 Core AMD Ryzen 3900XT CPU at 4.20GHz and 32GB of RAM.

2.1.6 Contact Interaction

Contact interaction was modeled between the carpal bones and the cartilage. The rigid carpal bones were specified as the master and the cartilage as the slave, based on the general rules for master and slave settings described in subsection 1.3.1. A surface-to-surface discretization method was selected, since it has shown to avoid pressure peaks in larger contact areas compared to node-to-surface discretization [15] (see Figure 2.7).

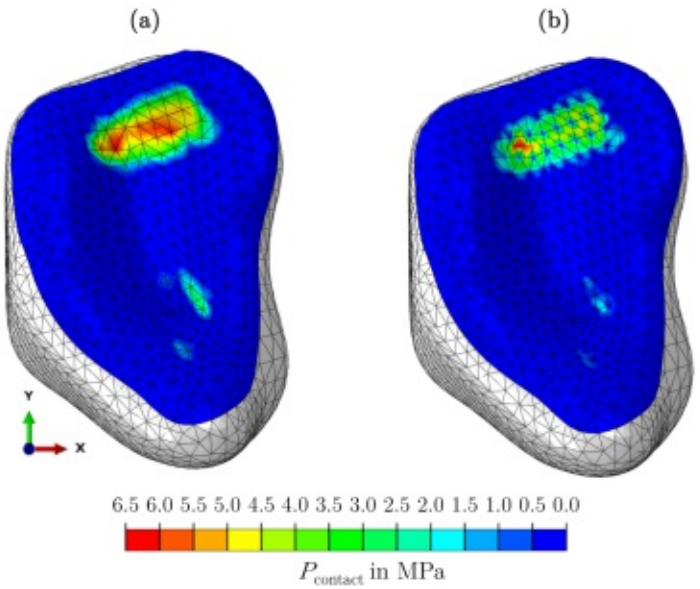

Figure 2.7: Comparison of different surface discretization methods in terms of contact pressure distribution; (a) surface-to-surface; (b) node-to-surface.

A finite-sliding formulation was chosen, since it was assumed that a given slave node might not always interacts with the same subset of master surface nodes. As a contact enforcement method, the augmented Lagrange multiplier method (see section 1.3.1) was chosen based on literature reference [8]. A hard pressure-overclosure relationship was utilized and tangential behavior was assumed as frictionless. The contact stiffness scale factor was set to one. The clearance, at which contact pressure was assumed, was set to zero ($p_0 = 0$). Separation of the contacting surfaces was allowed during contact to avoid overconstraint issues. Slave node adjustment was performed only to remove overclosure and to be precisely in contact with the master surface at the beginning of the analysis. There was no smoothing of any of the two contact surfaces performed.

Furthermore, the peak contact pressure (P_{peak}), mean contact pressure (P_{mean}) as well as the contact area (A_{contact}) of the reference model were calculated for each region corresponding to the respective bone in contact with the cartilage. A_{contact} was calculated as the sum of the contact area for each node involved in the contact interaction. Based on the coordinates of the deformed configuration of the model the area was further distinguished between area corresponding to the contact interaction of the lunate and the scaphoid. These values were further used for comparison of the reference model with similar models in the literature. A visual representation of the final reference model is given in Figure 2.8.

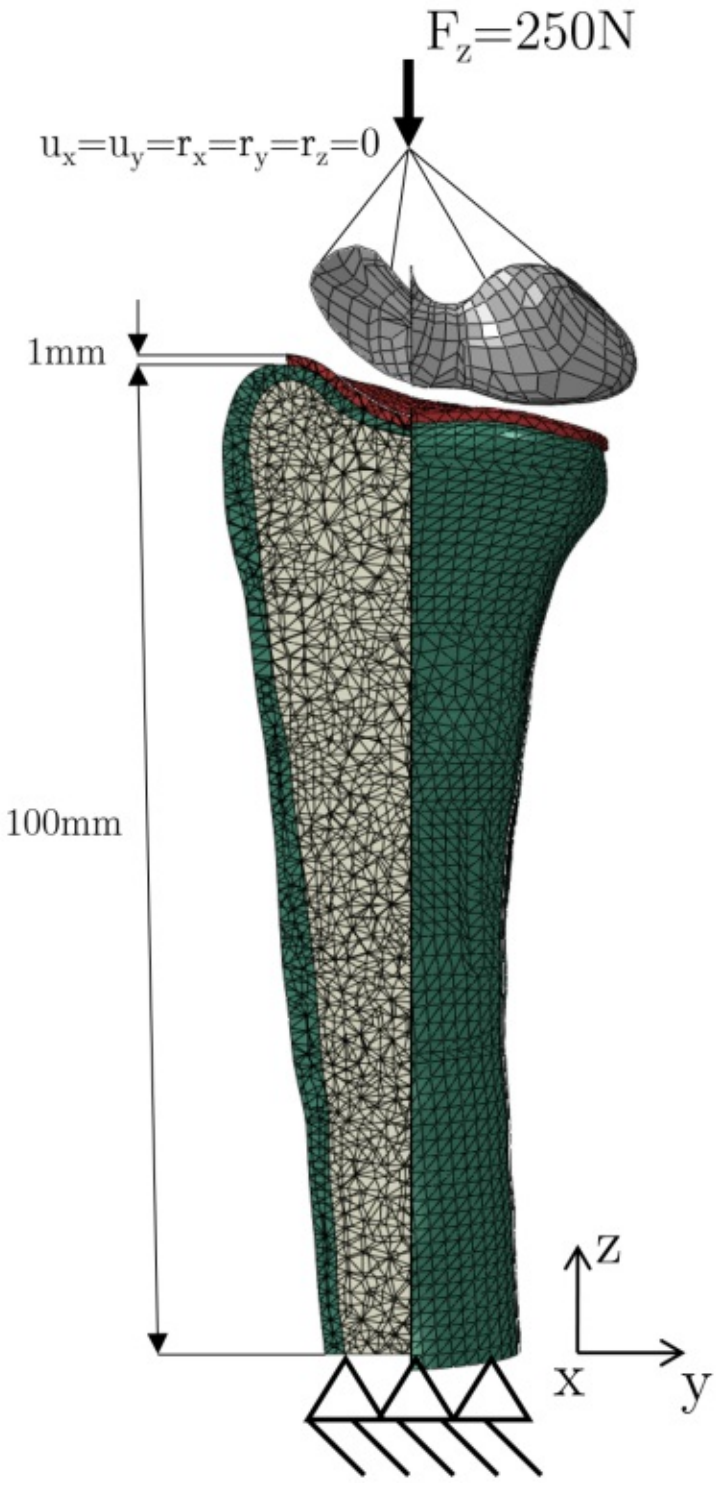

Figure 2.8: Visual representation of the reference model established with the presented workflow. The different parts of the model are marked by the following colors: green - cortex, grey - trabecular, red - cartilage and silver - carpal bones. $u_{x,y}$ and $r_{x,y,z}$ denote displacement and rotation in the specified direction, respectively.

2.2 Parameter Sensitivity Study

A parameter sensitivity study was performed to investigate the behavior of the reference model with respect to changes of its parameters. Therefore, a set of parameters was altered as given in Table 2.1. Bone material parameters were kept constant as the goal was to investigate mainly the effect of different BCs at the articular surface.

Table 2.1: Different parameters tested in the parameter sensitivity study for cartilage and contact interaction.

Cartilage				Contact enforcement method
Thickness	Materials		Element Types	
1.0mm*	Neo-Hookean hyperelastic*	E=10MPa*	C3D10 (Tet)*	Augmented Lagrange*
0.5mm	Elastic	E=5MPa	C3D4 (Tet)	Direct
2.0mm		E=10MPa	C3D8 (Hex)	Linear penalty
No cartilage	Neo-Hookean hyperelastic	E=5MPa	C3D20 (Hex)	Nonlinear penalty

* Parameters of the reference model

The thickness of the cartilage was altered and a model without cartilage was created. The thickness of the cartilage was decreased to 0.5mm as well as increased to 2.0mm. Due to the increase in thickness, there was no longer a single layer of elements (such as in the reference model) present in the model with 2mm thickness, but two.
Additionally, the influence of different cartilage material properties was investigated. Therefore, the material property was varied between an elastic and hyperelastic material and the Young's Modulus between 5.0 and 10.0MPa.
The mesh element types were changed to linear C3D4 tetrahedral and linear as well as quadratic hexahedral elements (types C3D8 and C3D20, respectively). Due to the change of the mesh of the cartilage, a tie constraint was used to tie the nodes of the cartilage's bottom and the articular surface of the radius together. In order to ensure comparability between the different cartilage mesh variations, the reference model was also remodeled with a tie constraint instead of a consistent mesh between cartilage and articular surface of the bone. The difference between the reference model with a tie constraint and without one was quantified by calculating the relative error between U_{mean} for both models. Since the error was smaller than 0.1% the model variation with a tie constraint was considered to represent the reference model well enough to be used in the parameter sensitivity study. Furthermore, the hexahedral meshing led to changes of the geometry of the cartilage due to the bottom-up meshing routine on the curved surface of the cartilage. A representation of the geometrical differences between the actual geometry and the resulting geometry of

the hexahedral mesh is displayed in Figure 2.9. The respective changes in volume due to the bottom-up meshing routine for the hexahedral elements is given in percent of relative difference to the mesh of the reference model and the underlying geometry (see Table 2.2).

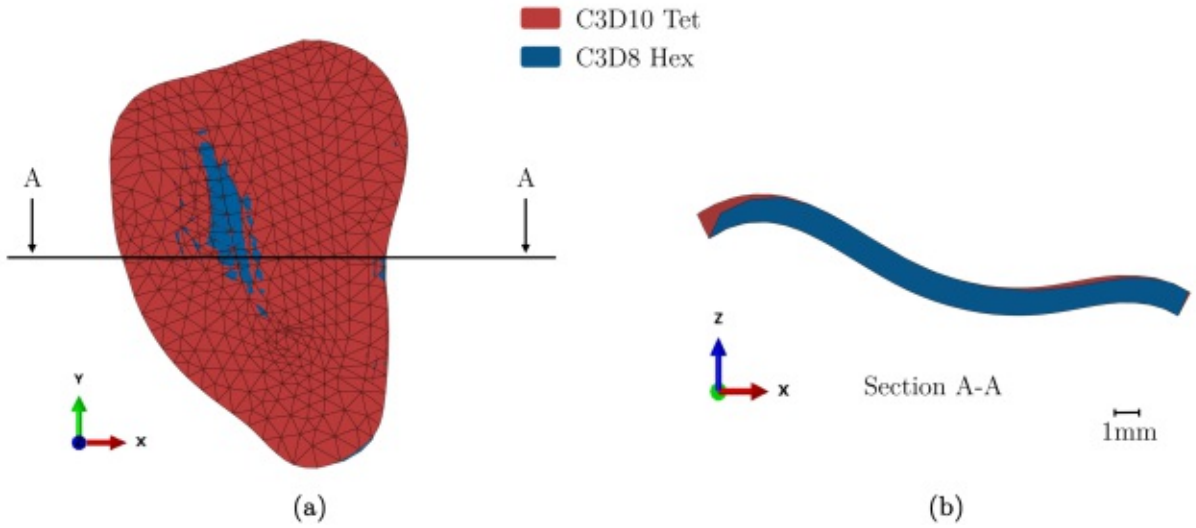

Figure 2.9: Differences in the geometry of the cartilage due to hexahedral mesh (blue) compared to the tetrahedral mesh of the reference model (red). (a) Top view and (b) section view of the cartilage.

Table 2.2: Volume and difference of volume in percent of the tetrahedral elements used in the reference model (C3D10) and the hexahedral elements for comparison (C3D8, C3D20).

	Geometry	C3D10 (Tet)*	C3D8 (Hex)	C3D20 (Hex)
Volume in mm^3	590	588	492	486
Difference to geometry in %		0.3	16.6	17.5

* Parameters of the reference model

Since no other meshing routine was possible to implement in the workflow, the differences in the volumes were taken into consideration in the interpretation of the results.
Finally, the influence of different contact enforcement methods was investigated. Therefore, the following methods were considered: the linear and nonlinear penalty methods (see subsection 1.3.1) as well as the direct method. These methods were chosen to compare a selection of the most commonly used contact enforcement methods. Furthermore, it was of interest, if the contact locations as well as the pressure distribution would differ, due to larger penetrations occurring in case of the use of the penalty method. The direct method is a particular method used in Abaqus and strictly enforces a hard pressure-overclosure relationship with the use of Lagrange multipliers.

2.2.1 Metrics of Comparison

An element wise comparison between different models was possible because all models in the parameter sensitivity study used the same mesh of the radius bone. For the parameter sensitivity study as well as the further model comparisons (which will be explained in detail in the following sections) the effective stress $\bar{\sigma}$ was used as an equivalent stress variable. It is defined as

$$\bar{\sigma} = \sqrt{2EU}, \tag{2.4}$$

where E denotes the Young's modulus and U the strain energy density from Equation (2.1). The effective stress was chosen, since in comparison with the von Mises equivalent stress, it takes into consideration both, the deviatoric as well as the volumetric part of the stress tensor [55].
To quantify the differences between different models, the root mean square error (RMSE) defined as

$$\mathrm{RMSE} = \sqrt{\frac{1}{n}\sum_{i=1}^{n}(\hat{y}_i - y_i)^2} \tag{2.5}$$

was used. Since an element wise comparison of the effective stress was performed, $\hat{y}$ and y denote the effective stress values of element i (at the centroid) of the reference model and the compared model, respectively and n denotes the number of elements in the region of comparison.
Given that the scale of the RMSE is dependent on the values of the data set used, normalization is often used to ensure meaningful comparison. Therefore, the RMSE was normalized by the maximum occurring effective stress in the reference model as

$$\mathrm{NRMSE}_{\mathrm{Region}} = \frac{\mathrm{RMSE}}{\bar{\sigma}_{\max}}, \tag{2.6}$$

where $\bar{\sigma}_{\max}$ is the maximum effective stress in the respective bone region of the reference model and is further referred to as the normalized root mean square error of the specific region ($\mathrm{NRMSE}_{\mathrm{Region}}$), for subchondral and Colles' fracture region. A detailed description of how these two regions were defined and elements were allocated to the each region is given in section 2.4.5.

2.3 Linearity of Subchondral Bone Stresses

Although, the reference model hosts nonlinear properties due to the application of the contact interaction between carpal bones and cartilage and the nonlinear cartilage material used, it could well be the case that the stresses inside the bone scale near linearly with an

increase in applied load. If the stresses inside the bone scale linearly, this would lay the foundation for simplified models without contact that are valid for more than just one load level. Therefore, an analysis of the linearity of subchondral bone stresses (inclduding the subchondral and the Colles' fracture region) was performed to assess whether the bone material shows a linear response to an increase of applied force.
This linearity analysis was conducted by applying three increased loads of 500N, 1000N and 3000N to the reference model, which was initially loaded with 250N. As a measure of linearity between these differently loaded models, a linear regression between the effective stresses was calculated for each possible combination of reference model and differently loaded models. To ensure comparability between the different load levels the effective stress was normalized as

$$\bar{\sigma}_{\text{norm}} = \frac{\bar{\sigma}}{F_z}, \tag{2.7}$$

where F_z is the respective load applied to the model.
Linear regression is used to model the relationship between a dependent variable y and one or more independent variables x using the least squares approach. This way the data is fit such that it can be explained with a linear equation (for example, a fitted line) defined as

$$y = x\beta + \epsilon, \tag{2.8}$$

where the dependent variable y is given by the independent variable x with the intercept of the line ϵ and slope β. The slope of the linear fit was used as an indicator of how linear the response of the differently loaded model in terms of the normalized effective stress inside the bone was. A slope of one would indicate a linear behavior since the normalized effective stresses would stay the same even if the model's load is increased (see Figure 2.10).

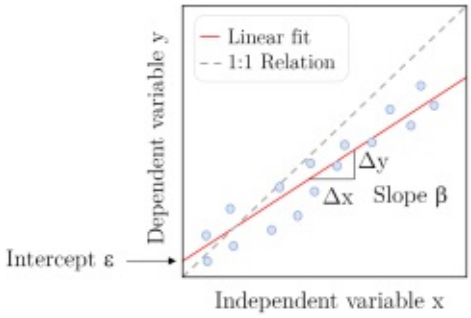

Figure 2.10: Example of a linear regression of dependent variable y, independent variable x, intercept ϵ and slope of the fitted line β. The linear fit is depicted in red and the perfect, 1:1 relation between two variables is shown as the dashed grey indicating a perfect linear relation.

The squared Pearson's correlation coefficient (R^2) was used to quantify how well the normalized effective stresses of the reference model and differently loaded models correlate with each other.

2.4 Simplified Models

To answer the research question of this thesis, i.e., to find out what level of detail regarding the BCs at the RCJ must be used to achieve a realistic representation of stresses in the subchondral and Colles' fracture region, models with an ascending level of complexity regarding their BCs were created to be compared to the reference model. Visual representations of the models of different complexity regarding their BCs are depicted in Figure 2.11 and details of the models are presented in the following subsections.

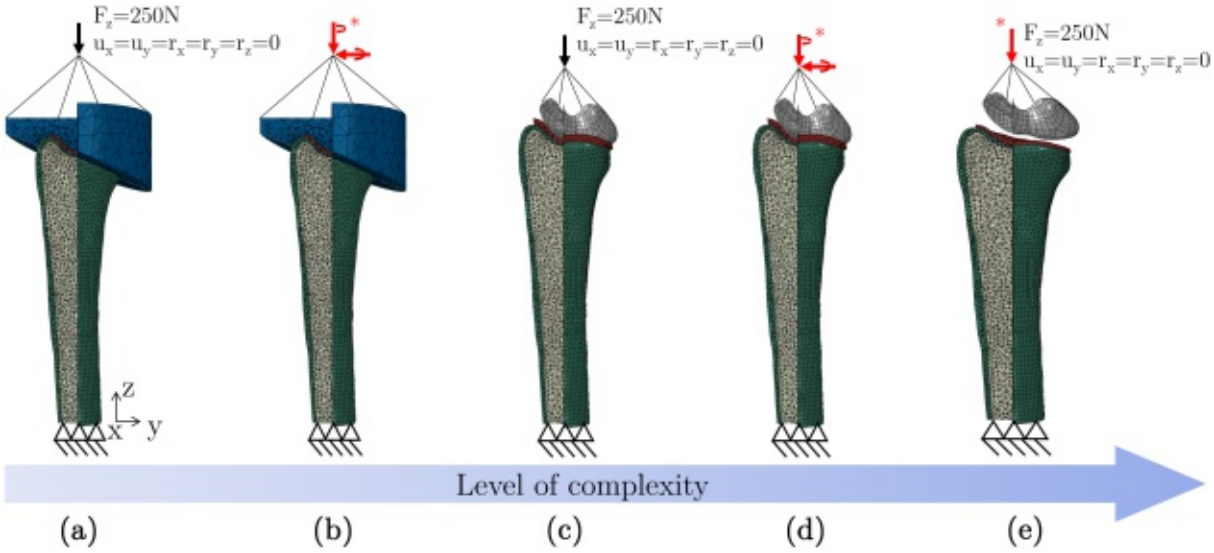

Figure 2.11: Level of complexity regarding the BCs of different models. (a) Embedded model with uniaxial load case (EM_u); (b) embedded model with multiaxial load case (EM_m); (c) model with bonded carpal bones and uniaxial load case (BM_u); (d) model with bonded carpal bones and multiaxial load case (BM_m); (e) reference model with contact interaction. Loads marked in red indicate statically equivalent loads calculated from the reference.

2.4.1 Embedded model uniaxially loaded (EM_u)

At the lower end of complexity, a model with an embedding was considered. This type of model was chosen to represent the simplest form of loading a radius experimentally. The embedding was modeled in Solidworks as a cylinder with a diameter of 50mm (see Figure 2.12c). The distal end of the radius was embedded approximately 1mm to the articular surface based on Muller et al. [5]. The embedding was meshed using C3D10 tetrahedral

elements with a mesh size of 5mm (see Figure 2.12a). The mesh was refined in the region in contact with the cartilage and radius meshes and therefore set to a mesh size of 0.5mm (see Figure 2.12b). These mesh settings resulted in 12247 elements for the embedding.

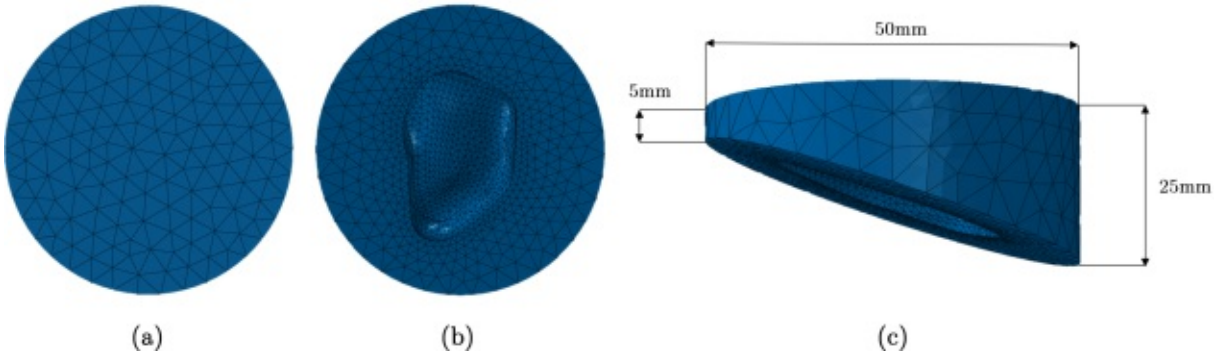

Figure 2.12: (a) Coarse mesh of the modeled embedding; (b) Mesh refinement at the interaction with the cartilage and radius; (c) Dimensions of the embedding.

The material of the embedding was assumed to be a polyurethane with E=1.45GPa and ν=0.3 based on Synek et al. [38]. The embedding was connected to the radius and cartilage using a tie constraint to ensure no changes to the present mesh of the radius for further comparisons of the embedded model (EM) with the reference model. Furthermore, the cartilage was left as part of the EM as a hyperelastic neo-Hookean material with the same material parameters as previously described in section 2.1.4. Hence, consistency in terms of comparison between the different models was given. A reference point was set 30mm distally on the z-axis of the model and was connected via a multi-point beam constraint with the top surface nodes of the embedding.
The displacement and rotation at the reference node were coupled to the displacement and rotation at the designated nodes of the embedding, corresponding to the presence of a rigid beam between them [15]. At the proximal end of the bone, all nodes of the bottom surface were constrained using an encastre, identically to the BC of the reference model. The EM was loaded at the reference point uniaxially with a force of F_z=250N and all DoFs except for the displacement along the z-axis were locked. It is therefore further referred to as the uniaxially loaded embedded model (EM_u).

2.4.2 Embedded model multiaxially loaded (EM_m)

Since reaction forces between the reference model and the EM_u might turn out differently, another EM was created with reaction forces and moments which are statically equivalent to those of the reference model. Given that off axis loading might be applied to the radius in the reference model due to the physiological alignment of the carpal bones and therefore to ensure better comparability of the simplified models with the reference model, a second loading case was developed for the EM. Hence, the idea of the second created

load case for the EM_u was a model with statically equivalent reaction forces and moments at the proximal end of the bone when compared to the reference model. Therefore, the following was considered: the necessary forces and moments to be applied at the reference node of the embedded model were calculated based on the undeformed model geometry and static equilibrium equations. In a first step the reference model was solved and the reaction forces and moments at the encastre were evaluated. Then these reaction forces and moments were used in the equilibrium equations established at the origin of the global coordinate system as given in Equation (2.9) to calculate the forces and moments present at the reference point of the undeformed uniaxially loaded EM_u.

$$\sum F^{\text{Encastre}}_{\text{Reference}} = \sum F^{\text{Encastre}}_{\text{EM}} \quad \text{and} \quad \sum M^{\text{Encastre}}_{\text{Reference}} = \sum M^{\text{Encastre}}_{\text{EM}} \tag{2.9}$$

The EM model was then loaded with these forces and moments at the reference point and is further referred to as the multiaxially loaded EM (EM_m). Given that the EM_m deformed differently loaded in this state, a small error in the resulting reaction forces and moments at the encastre was introduced via this method. Nevertheless, this error was assumed as negligibly small, amounting to 0.1 and 2.2% in terms of reaction forces and moments, respectively. Except for the loading at the reference point, the EM_m model used the same parameters as the EM_u model.

2.4.3 Bonded carpals model uniaxially loaded (BM_u)

Increasing the complexity level of BCs, a model in which the carpal bones were connected directly via a tie constraint to the cartilage was chosen. For the bonded model (BM), the cartilage was again assumed as a hyperelastic neo-Hookean material with E=10MPa and ν=0.45 (as described in section 2.1.4 in detail). The cartilage was extruded in Solidworks until it reached the bottom surface of the carpal bones, such that the carpal bones were embedded within the cartilage (see Figure 2.13).
Hence, no contact conditions were applied, but a tie constraint was set between the top nodes of the cartilage and the bottom nodes of the carpal bones. Again, the BM was loaded at the reference point uniaxially with a force of F_z=250N and all DoFs except for the displacement along the z-axis were locked. At the proximal end, all nodes of the bottom surface were constrained using an encastre, identically to the BC of the reference model.

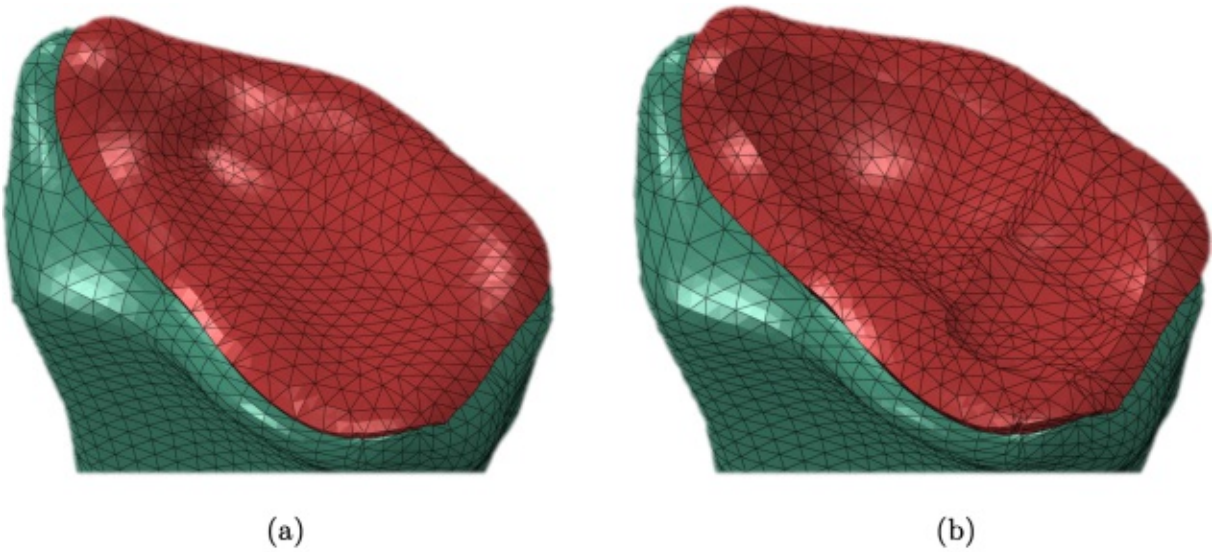

Figure 2.13: (a) Cartilage of the reference model extruded by 1mm in local normal direction on the articular surface; (b) Cartilage of the BM extruded to the surface of the carpal bones.

2.4.4 Bonded carpals model multiaxially loaded (BM_m)

At the last stage of complexity regarding the BCs, the BM_u was loaded multiaxially just as described in the above paragraph regarding the EM_m. The remaining parameters of the model were kept identical to the BM_u model.

2.4.5 Comparison with Reference Model

The two regions of interest - subchondral and Colles' fracture region - were defined based on the work of Eastell et al. [56], at 22 ± 4mm proximal from the tip of the radial styloid process. Therefore, the subchondral region was set from the tip of the radial styloid process until 18mm proximal. The adjacent region of 8mm was marked as the Colles' fracture region (see Figure 2.14). Elements were allocated to the specified region based on their element centroid coordinates along the z-axis. Therefore, elements intersected by the border of the two regions were allocated to the specified region if their element centroid was located in the specified region.

As described in section 2.2.1, the effective stress was used as the mechanical parameter of comparison. The element wise normalized root mean square error (NRMSE) was used to compare the reference model to the simplified models in a similar way as described in section 2.2.1. An element wise comparison between different models was possible because all models used the same mesh of the radius bone. The RMSE was calculated for slices of 1mm along the longitudinal z-axis of the bone (see in Figure 2.15). Then, the NRMSE of each 1mm section was calculated by dividing the RMSE by the respective $\bar{\sigma}_{max}$ of each

1mm section for each bone region, trabecular and cortex. This NRMSE calculated for each slice of 1mm was then further referred to as the $NRMSE_{Slice}$.

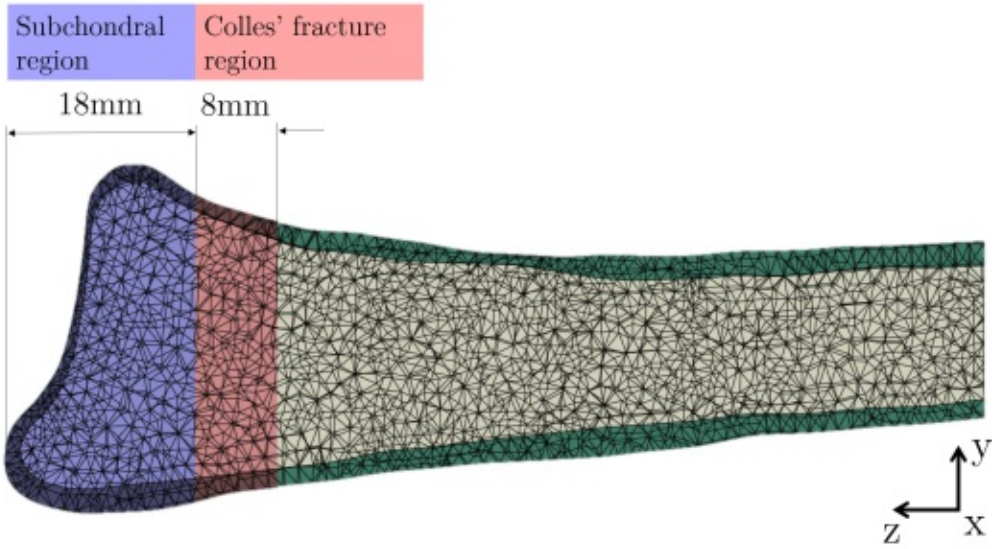

Figure 2.14: Schematic representation of the Colles' fracture and subchondral regions along the vertical z-axis of the bone.

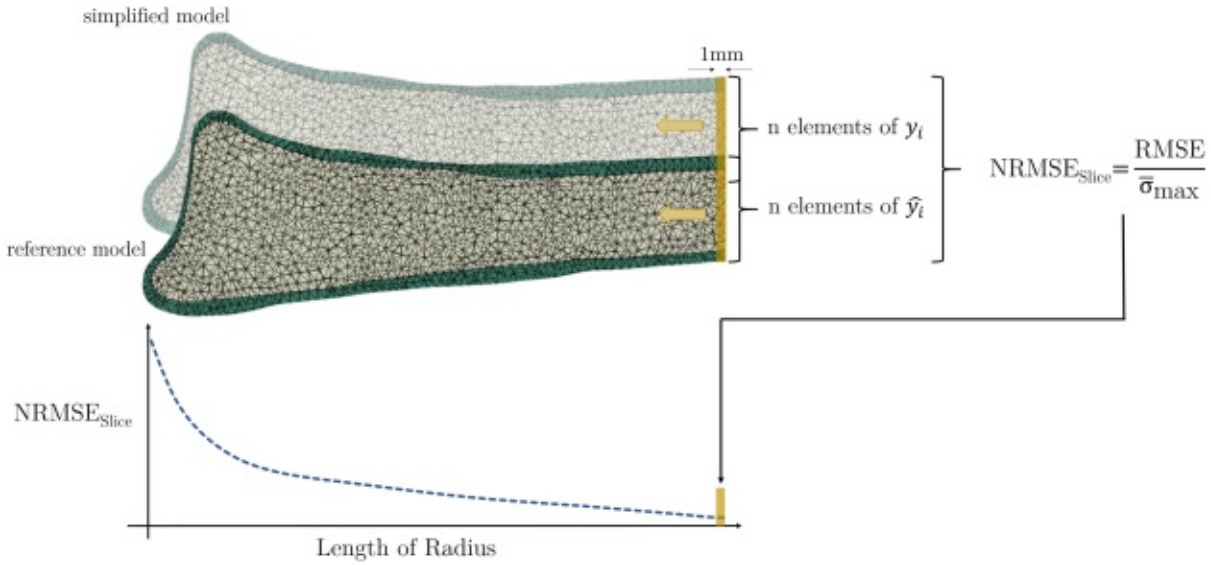

Figure 2.15: Schematic representation of the calculation of the $NRMSE_{Slice}$ between the reference model and one of the simplified models based on equation 2.5.

Additionally, the maximum $NRMSE_{Slice}$ was calculated for subchondral and Colle's fracture region individually as the maximum occurring $NRMSE_{Slice}$ and is further referred to as $NRMSE_{Slice,max}$.

Furthermore, the NRMSE was calculated for the entire subchondral and Colles' fracture regions. The RMSE of each region was calculated and further normalized by division of

the the respective $\bar{\sigma}_{\max}$ of the region. This parameter was therefore referred to as the $\text{NRMSE}_{\text{Region}}$.
Through the use of this method, the different regions of interest - subchondral and Colles' fracture region - could be compared between different models and the reference model.

3 Results

The results are structured according to the presented methodology in chapter 2. First, the results regarding the reference model are given and compared to similar models in the literature (see section 3.1). Second, the results of the parameter sensitivity study are shown (see section 3.2) followed by the results of the analysis of the linearity of the subchondral bone stresses of the reference model (see section 3.3). Last, the comparison of the reference model with the simplified models is displayed comprised of qualitative and quantitative results (see section 3.4).

3.1 Reference Model

In this section the results of the reference model of section 2.1 are presented and compared to similar models in the literature. The section is divided into qualitative and quantitative results. Regarding the qualitative results, contour plots of the effective stress on the articular surface of the bone (see Figure 3.1 and along the view cut of the z-y-plane of the bone (see Figure 3.1b) are displayed.

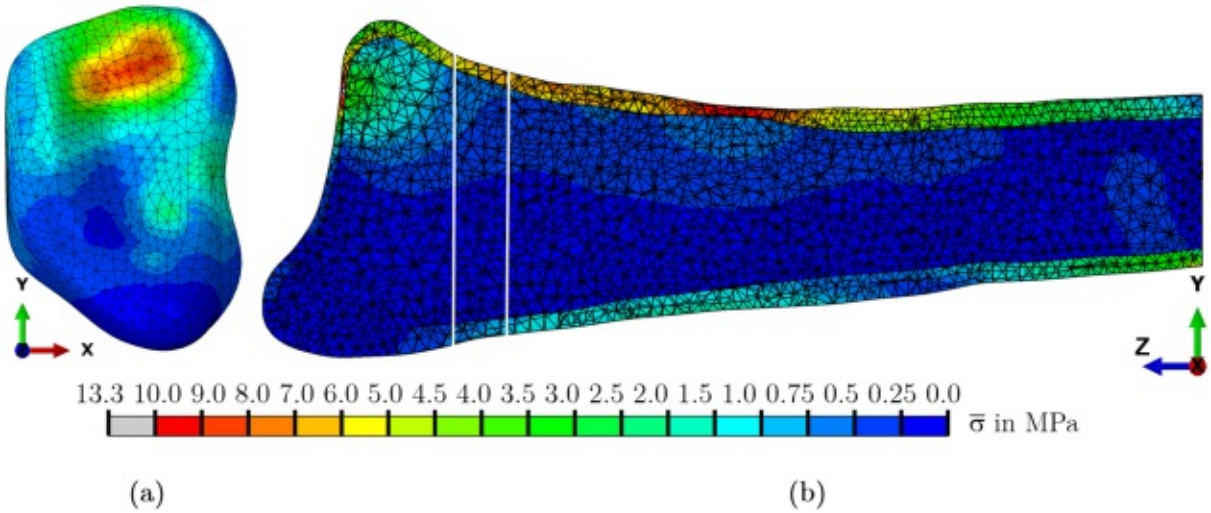

Figure 3.1: (a) Contour plots of the effective stress ($\bar{\sigma}$) in MPa on the articular surface of the bone and along the view cut of the z-y-plane of the bone (b). White vertical lines distinct the subchondral from the Colles' fracture region.

As shown in the contour plots of the effective stress, a load transfer from the cortex to the subchondral trabecular region occurred, despite the presence of cartilage between radius and carpal bones. An uneven load distribution between the lunate and scpahoid is present due to contact between the carpal bones and the cartilage. Furthermore, the effective stress is strongly represented in the subchondral trabecular region and greatly decays towards the beginning of the Colles' fracture region. Effective stress distribution in the cortex is greatest in the mid region of the radius where the diameter of the bone is decreased in relation to the distal region and the cortex is thin. Due to the placement of the carpal bones, effective stress is mostly present ulnar at the radius. P_{peak}, P_{mean} as well as A_{contact} of the reference model are listed in Table 3.1 for further comparison. These values were used for comparison of the reference model with similar models in the literature.

Table 3.1: Peak contact pressure (P_{peak}), mean contact pressure (P_{mean}) and contact area (A_{contact}) of the scaphoid, lunate and in total for the reference model. The share of the total values for each carpal bone are displayed in brackets in percent.

	Scaphoid	Lunate	Total
A_{contact} in mm^2	21.10 (33%)	42.18 (67%)	63.28
P_{peak} in MPa	3.59	7.15	7.15
P_{mean} in MPa	0.31 (±1.08)	0.37 (±1.24)	0.34 (±1.17)

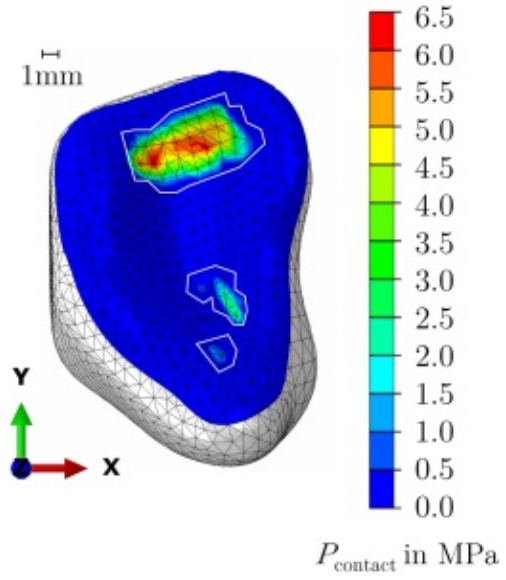

Figure 3.2: Contour plot of the contact pressure (P_{contact}) of the cartilage surface. The white outlines mark the region at which $P_{\text{contact}} > 0$. A length scale of 1mm is given as a reference for the contact area.

The contact area of the reference model was 63.28mm^2, with 33% and 67% accounting to the scaphoid and lunate, respectively. The P_{peak} was 3.59MPa at the scaphoid and 7.15MPa at the lunate.
Regarding the contact pressure and its distribution on the surface of the cartilage, they are shifted more towards the lunate region rather than the scaphoid (see Figure 3.2).

3.2 Parameter Sensitivity Study

The results of the parameter sensitivity study are presented in the result section divided in two parts. First, there is the qualitative comparison of contour plots. Second, there is the quantitative comparison of the element wise $\text{NRMSE}_{\text{Region}}$ for the subchondral and Colles' fracture regions., which was calculated as described in section 2.2, for all tested parameters compared to the reference model (see Figure 3.3). The two bone regions, cortex and trabecular, are displayed in separate rows of the plots.

Quantitative results

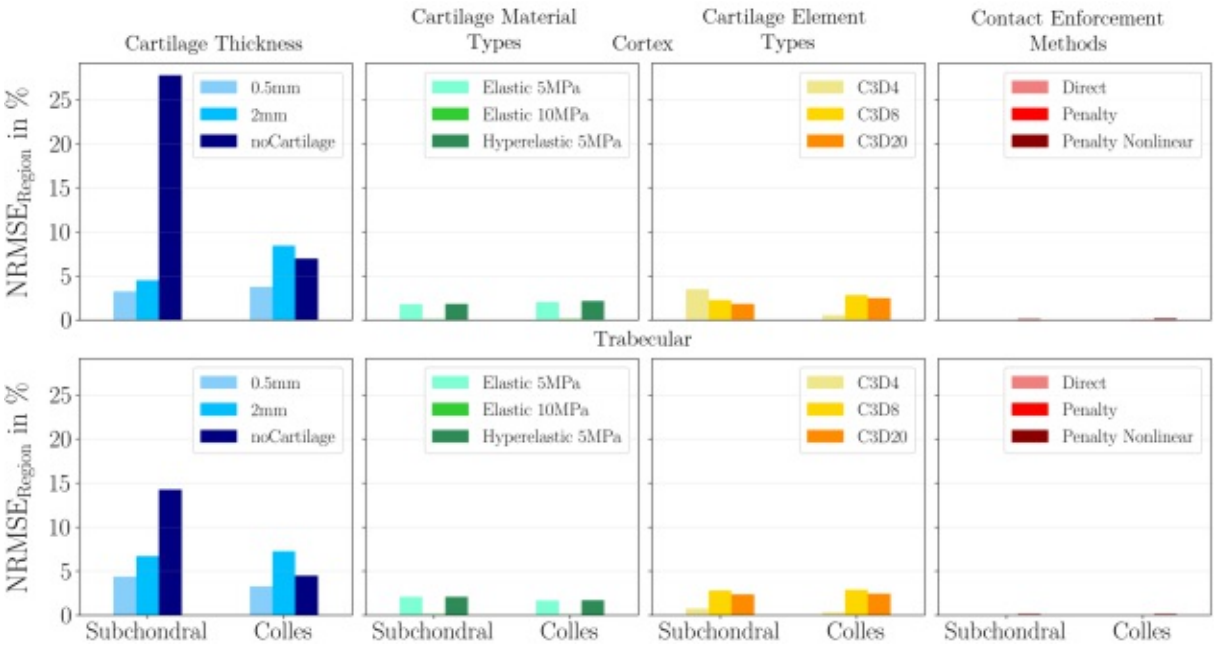

Figure 3.3: $\text{NRMSE}_{\text{Region}}$ in % of the subchondral and Colles' fracture regions (cortex and trabecular) for a change in cartilage thickness (shades of blue), cartilage material type (shades of green), cartilage element type (shades of yellow) and used contact enforcement method (shades of red).

The $\text{NRMSE}_{\text{Region}}$ for a change in cartilage thickness was the greatest in the subchondral region if no cartilage was used (28% and 14% for cortex and trabecular region, respectively).

In the Colles' fracture region an increase to 2mm of cartilage thickness showed the largest differences (8% and 7% for cortex and trabecular regions, respectively).
Regarding a change of the used material for the cartilage, the results were similar in both regions, subchondral and Colles' fracture region. A change in Young's modulus from 10MPa to 5MPa led to a $NRMSE_{Region}$ of 2% in both the cortex and the trabecular bone. Changing the material from an elastic to a hyperelastic material on the other hand, showed almost no $NRMSE_{Region}$ compared to the reference model.
In terms of a change of the used element type for modeling the cartilage, the use of hexahedral elements resulted in a $NRMSE_{Region}$ of 2% and 3% (C3D8 and C3D20, respectively) for the cortex and 3% and 2% for the trabecular region. There was almost no $NRMSE_{Region}$, if a linear tetrahedral element type (C3D4) was used, except for the subchondral cortex region.
The use of different contact enforcement methods in Abaqus showed almost no differences in terms of $NRMSE_{Region}$. Only the use of the nonlinear penalty method resulted in minor $NRMSE_{Region}$ of 0.1% and 0.01% for the cortex and trabecular region, respectively.

Qualitative results

Qualitative plots of the effective stresses of the models with different cartilage thicknesses are given in Figure 3.4, since a variation of this parameter showed the largest differences compared to the reference model of all four parameters. The contour plots of the remaining parameters, which were investigated as part of the parameter sensitivity study, are given in the supplementary material (4.6).
The qualitative results showed that the thicker the cartilage, the bigger the shift of the load distribution away from the lunate towards the scaphoid. Therefore, the load is distributed more evenly on the articular surface along the cortex and the stress concentration underneath the contact location of the lunate in the subchondral trabecular region is greatly reduced. Furthermore, there was almost no load transferred through the lunate if no cartilage was used.

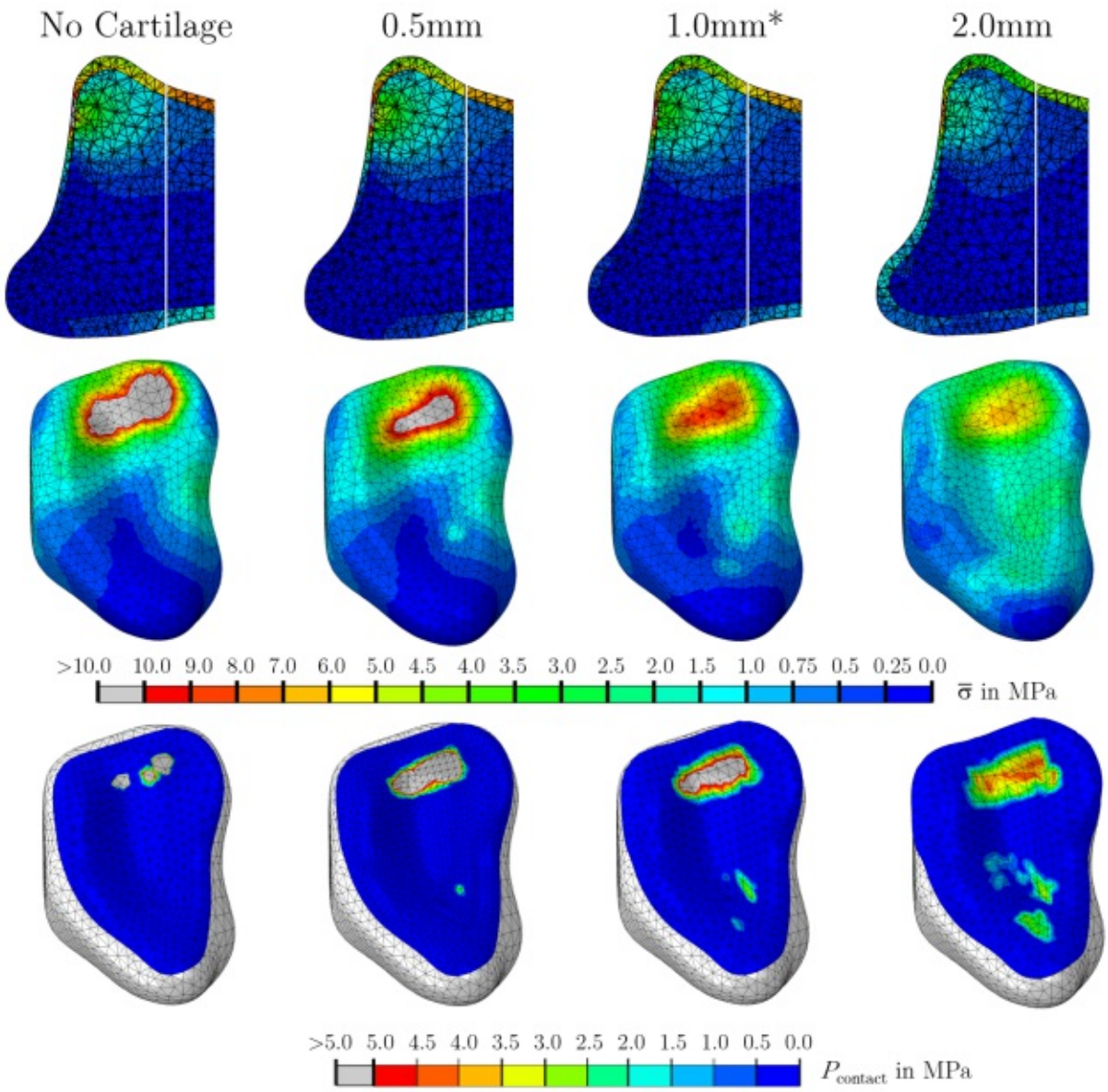

Figure 3.4: Qualitative contour plots of the effective stress ($\bar{\sigma}$) in MPa of the models with 0.5mm, 1.0mm (=reference model), 2mm and no cartilage. The top row shows the view cut of the z-y-plane including the subchondral as well as the Colles' fracture region. The second row shows the view of the articular surface of the bone. The third row displays the contact pressure on the cartilage.

3.3 Linearity of Subchondral Bone Stresses

The results of the linear regression analyses, which were calculated as described in section 2.3, are displayed as scatter plots of the compared data and the line of best fit in Figure 3.5. All combinations of differently loaded models and the reference model are shown. The plots are separated between the two bone regions, cortex and trabecular. Slope, intercept,

R^2 and p-values of the linear regressions between the differently loaded models are given in Table 3.2 for further comparison.

Table 3.2: Slope, intercept, R^2 and p-values of the linear regression analyses for cortex and trabecular region for all different combinations of load levels of 250N, 500N, 1000N and 3000N. Redundant combinations were not considered.

Cortex												
	500N				1000N				3000N			
	Slope	Intercept	R^2	p	Slope	Intercept	R^2	p	Slope	Intercept	R^2	p
250N	1.112	0.000	0.99	<0.000	1.119	0.001	0.97	<0.000	1.209	0.001	0.93	<0.000
500N					1.093	0.000	0.99	<0.000	1.117	0.000	0.96	<0.000
1000N									1.038	0.000	0.99	<0.000
Trabecular												
	500N				1000N				3000N			
	Slope	Intercept	R^2	p	Slope	Intercept	R^2	p	Slope	Intercept	R^2	p
250N	1.151	0.000	0.99	<0.000	1.303	0.000	0.98	<0.000	1.426	0.001	0.94	<0.000
500N					1.144	0.000	0.99	<0.000	1.265	0.002	0.97	<0.000
1000N									1.123	0.000	0.99	<0.000

An increase in applied force led to an increase of deviations compared with the reference model, which manifested in a increase of the slope of the fitted line from 1.112 to 1.209 for the cortex and 1.151 to 1.426 for the trabecular region. Furthermore, R^2 decreased from 0.99 to 0.93 and from 0.99 to 0.94 (cortex and trabecular, respectively) with an increase in applied force.

From 500N to 1000N this increase was further increased with a slope of 1.093 for the cortex as well as 1.144 for the trabecular region.

At the last load increase, from 1000N to 3000N, the linear regression showed a slope of 1.038 and 1.123 for cortex and trabecular, respectively. This suggests that the model scales nonlinearly with increased applied force.

Furthermore, the contour plots of the contact pressure P_{contact} and the view cut of the normalized effective stress are displayed in Figure 3.6. The plots show that not only P_{contact} increased with increasing loads but also the contact area due to increased deformation of the cartilage. Additionally, the contact location of the scaphoid is stronger represented the more load is applied. Due to this shift of load transmission, the stress peak underneath the contact location of the lunate in the subchondral trabecular region is decreased with increasing loads.

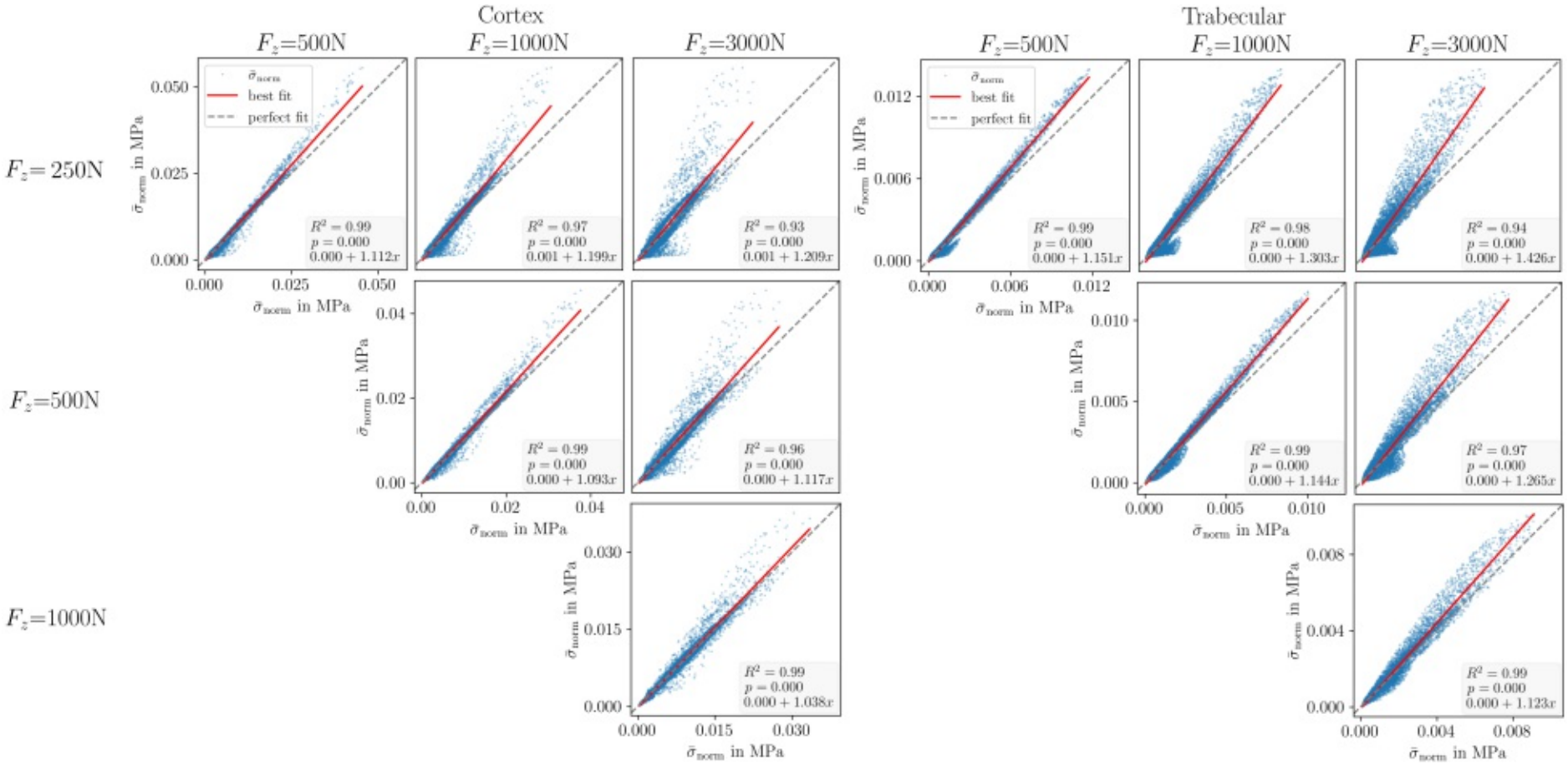

Figure 3.5: Linear regression models between the normalized effective stresses ($\bar{\sigma}_{norm}$) in MPa of differently loaded models for cortex and trabecular region. Redundant combinations were not considered. The x axes of the plots show the normalized effective stresses of the models loaded with 500N, 1000N and 3000N while the y axes show the normalized effective stresses of the models loaded with 250N, 500N and 1000N.

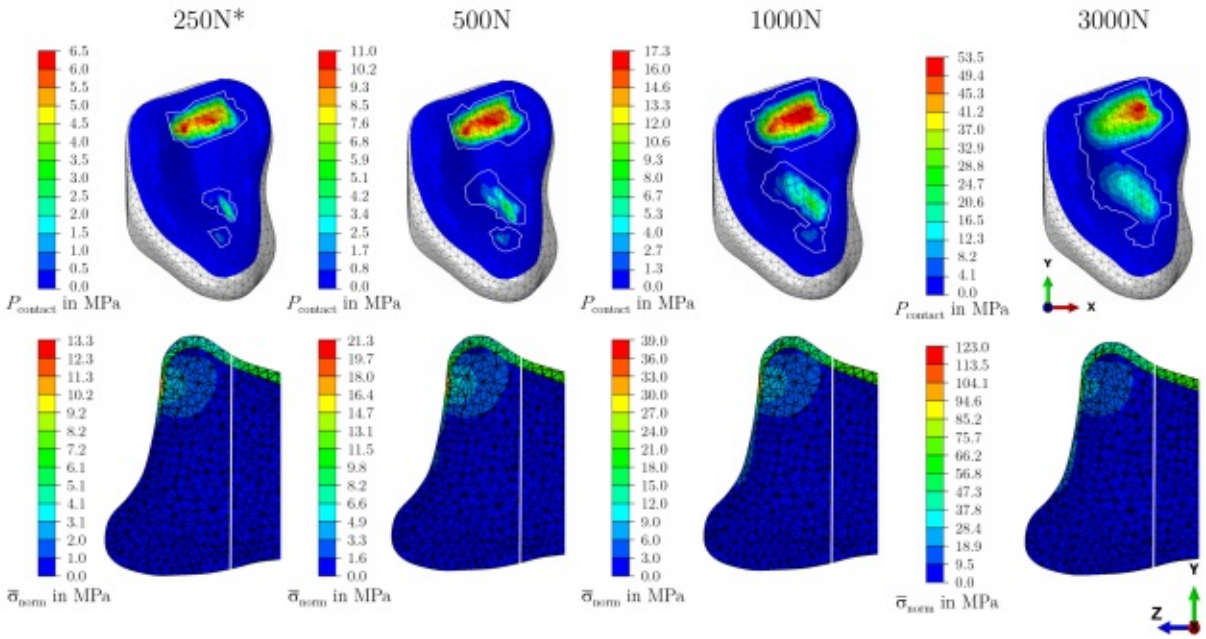

Figure 3.6: Contour plots of the cartilage contact pressure (P_{contact}) in MPa and the view cut of the normalized effective stress ($\bar{\sigma}_{\text{norm}}$) in MPa between the reference model (250N*) and the models with increased loads of 500N, 1000N and 3000N.

3.4 Comparison of Reference Model to Simplified Models

The comparison of the different simplified models described in section 2.4 is presented in the result section divided in two parts. First there is the qualitative comparison of contour plots. Second there is the quantitative comparison of the $\text{NRMSE}_{\text{Slice}}$ in sections of 1mm along the bone and $\text{NRMSE}_{\text{Region}}$ in the subchondral and Colles fracture region (explained in detail in section 2.4.5).

Qualitative comparison

For the qualitative comparison of the reference model and the simplified models the contour plots of the effective stress $\bar{\sigma}$ within the bone are presented in Figure 3.7. A view cut of the z-y-plane of the bone as well as a top view onto the articular surface of the bone are given.

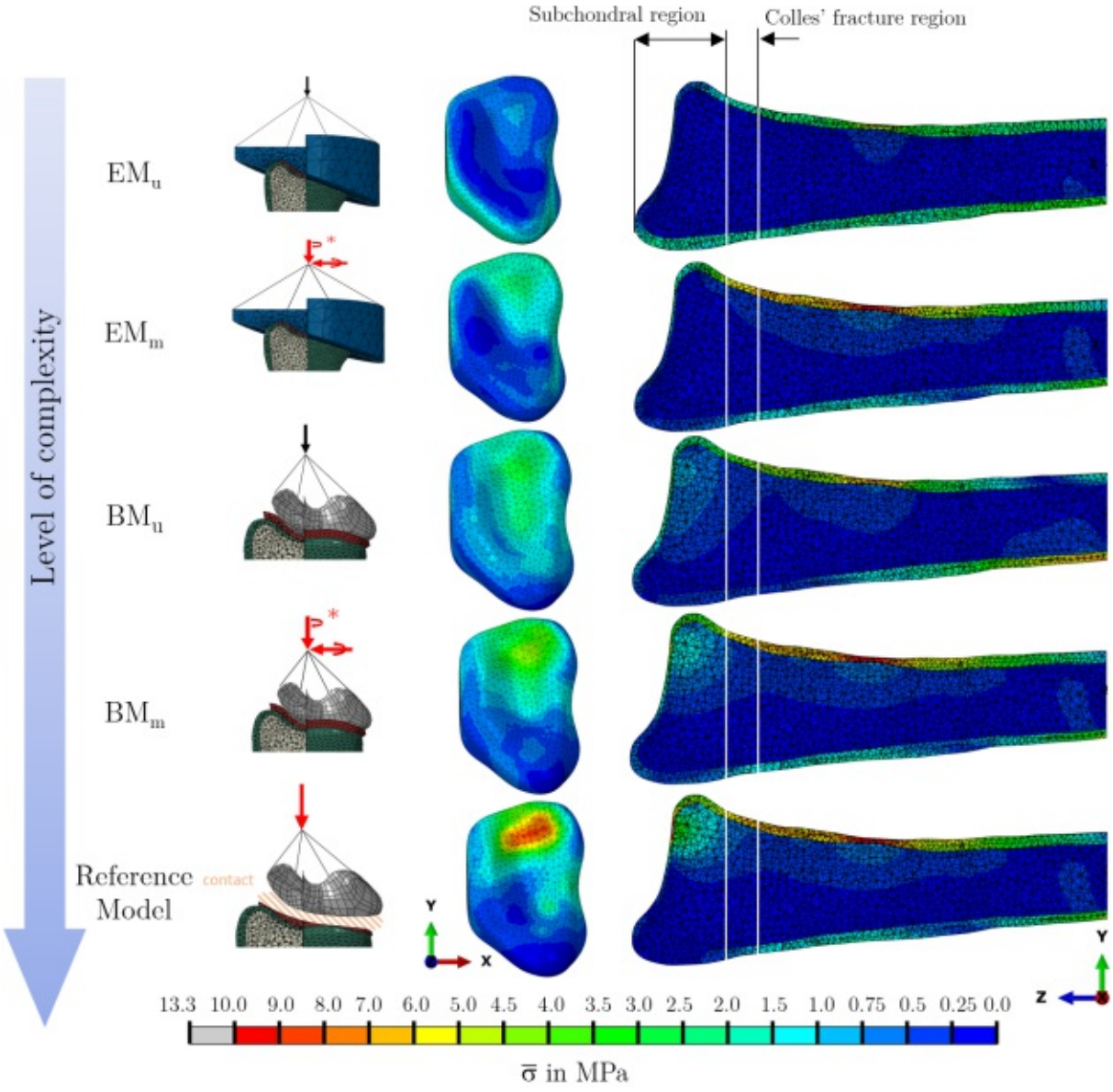

Figure 3.7: Contour plots of the effective stress ($\bar{\sigma}$) in MPa of the reference model and the different simplified models. Plots are listed in order of ascending complexity regarding their BCs. Vertical (along the y-axis) white lines on the contour plots distinguish the subchondral from the Colles' fracture region. Loads marked in red indicate statically equivalent loads calculated from the reference.

The qualitative comparison of the contour plots showed that more complex the BCs, the more pronounced stress concentrations in the subchondral trabecular region. Regarding the EMs, the stresses were almost entirely transferred via the cortical bone, effectively unloading the trabecular region. If statically equivalent loads were applied, in case of the EM_m, the stress distribution in the cortex resembled the reference model. For both EMs, the stresses in the trabecular region did not reach into the Colles' fracture.
Regarding the BMs stress transferred into the subchondral trabecular region, which increased if statically equivalent loads were applied (BM_m) but was underestimated compared to the reference model. The stresses in the cortex again resembled the distribution of stresses in the cortex of the reference model if statically equivalent loads were applied. Stresses induced through load transmission of the carpal bones in the trabecular have almost completely decayed when reaching the Colles' fracture region for the BM_u but started to reach the Colles' fracture region once statically equivalent loads were applied (BM_m). Stresses were more homogeneous on the articular surface of the bone in case of the BM_u.
Through the multiaxial load case as well as the contact interaction of the reference model, a bending moment was introduced, which manifests in stress concentrations in the mid region of the cortex.

Quantitative comparison

Regarding the quantitative comparison of the reference model and the simplified models, the $NRMSE_{Slice}$ of the effective stress along the bone is presented in Figure 3.8.
The course of the $NRMSE_{Slice}$ from distal to proximal showed a prominent peak in the subchondral region for all simplified models for cortex and trabecular regions and declined for the EM_m and BM_m towards the proximal end. The $NRMSE_{Slice}$ of the uniaxially loaded models EM_u and BM_u increased again after the subchondral and Colles' fracture region towards the proximal end for the cortex region and was comparably steady over its course for the trabecular region.
The $NRMSE_{Slice}$ peaks in the subchondral region were the largest for the EM_u ($NRMSE_{Slice,max}$ = 23% and 22%, cortex and trabecular region, respectively) and the smallest for the BM_m ($NRMSE_{Slice,max}$ = 14% for bothe the cortex and trabecular region)

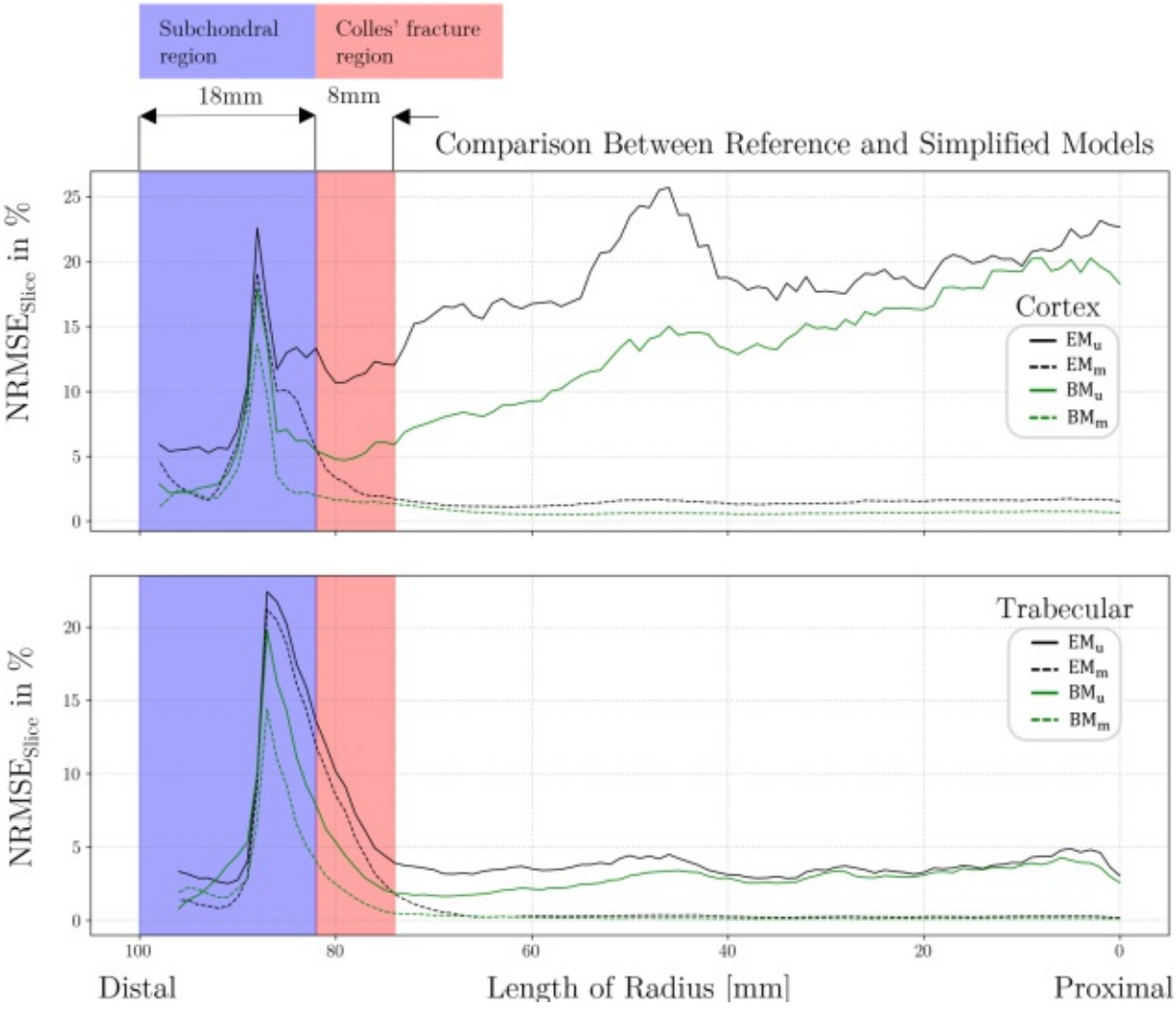

Figure 3.8: Normalized root mean square error ($NRMSE_{Slice}$) in % of the effective stress along the bone in sections of 1mm between reference model and the simplified models (EM_u, EM_m, BM_u and BM_m) for cortex and trabecular region.

The $NRMSE_{Slice,\ max}$ and the $NRMSE_{Region}$ are further displayed in a bar chart for subchondral and Colles' fracture region and cortex and trabecular regions, respectively (see Figure 3.9).

While in the subchondral region the $NRMSE_{Slice,\ max}$ was larger for all models than the $NRMSE_{Region}$, in the Colles' fracture region it was the other way around. Therefore, it can be stated that locally there were larger differences in the subchondral region observed compared to the Colles' fracture region for all different models.

Furthermore, the $NRMSE_{Region}$ for most models was smaller in the subchondral region compared to the Colles' fracture region. On the other hand, the $NRMSE_{Slice,\ max}$ was larger in the subchondral region compared to the Colles' fracture region.

Additionally, in the subchondral as well as the Colles' fracture region the difference compared to the reference model was the smallest for the most complex model (BM_m).

For all models the errors in the trabecular region decreased in the subchondral as well as the Colles' fracture region with increasing complexity of BCs.
Furthermore, in the Colles' fracture region the smallest difference was observed for the multiaxially loaded model with carpal bones (BM_m), in particular in the cortex of the bone.

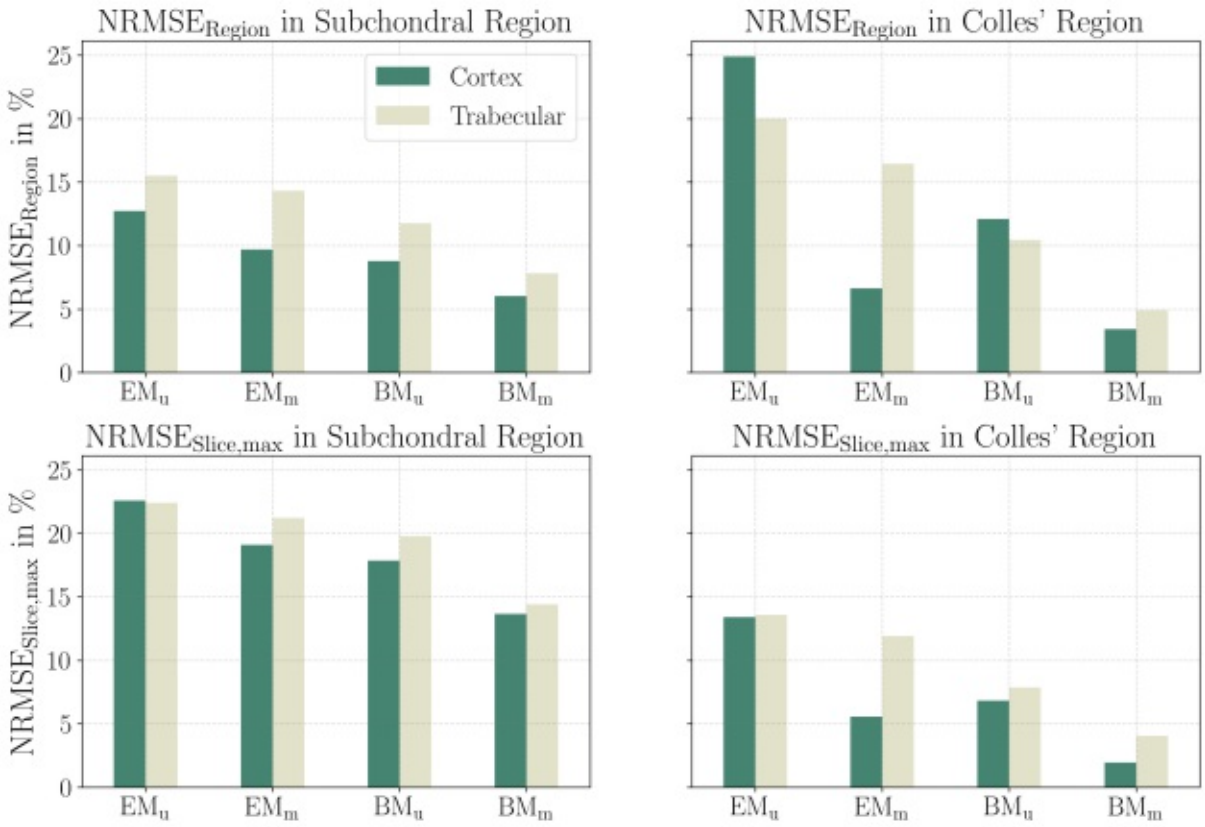

Figure 3.9: $NRMSE_{Region}$ and $NRMSE_{Slice,\,max}$ in % between the reference model and simplified models (EM_u, EM_m, BM_u and BM_m) for subchondral and Colles' fracture regions.

4 Discussion

This thesis addressed the question what level of detail regarding the BCs at the RCJ must be used to achieve a realistic representation of stresses in the subchondral and Colles' fracture region? A reference model of the distal radius with articular loading and contact interaction was established and compared to models with simplified BCs (an embedded model and one with the carpal bones bonded to the radius). The comparison with the reference model showed that the more complex the applied BCs, the stronger pronounced the stress concentrations in the subchondral trabecular region. If correct reaction forces and moments are known and the region of interest lies within the Colles' fracture region, a large simplification of BCs such as in the EMs can be utilized. If the stress distribution in the subchondral region is of interest, the application of statically equivalent loads and load transmission through carpal bones do not represent stress peaks sufficiently compared to a contact model and an error is unavoidable.

4.1 Reference Model

The results of the reference model showed increased stress concentrations in the trabecular subchondral region underneath the articular surface. These stresses were transferred via the cortical bone into the trabecular region, as a result of the contact interaction, placing increased structural demands in that area. The effective stress in the subchondral trabecular region decayed towards the Colles' fracture region, which leads to the assumption that this region is at the distance at which the Saint-Venant's principle applies.
The distinct stress concentrations in the subchondral trabecular region allow the assumption that implant design and arrangement in the trabecular bone could be affected by different loading mechanisms.
An uneven load distribution between the lunate and scpahoid was observed due to contact between the carpal bones and the cartilage. The load was shifted towards the lunate rather than the scaphoid. Although, in a majority of studies regarding contact interaction in the RCJ [57–59] the load distribution in the RCJ contact interaction is dominated by the scaphoid, the behavior of the reference model has also been seen in other studies such as by Johnson et al. [60]. In this study the authors validated their RCJ contact models

and found a shift towards the lunate for one out of three specimens. Hence, the load share of lunate and scaphoid was considered plausible in this work.
Furthermore, mean as well as peak contact pressure seemed reasonable in comparison with studies, using similar FE models, but different load levels. Johnson et al. [60] found contact forces in the range of 15 to 45N and 27 to 44N for lunate and scaphoid contact with an applied force of 110N, respectively. Furthermore, the authors of the same study found peak contact pressures in the range of 2 to 4 MPa, which corresponds with the peak contact pressure in the reference model of this study, given around two times the applied force. Additionally, two other studies [58, 59] found very similar results in terms of peak contact pressure. A study by Varga et al. [50] found contact forces of around 7N for a contact area of 27mm^2 in the loaded neutral position of the RCJ, which corresponds well with the magnitude of the mean contact pressure of the reference model.
While there are FE studies serving as a comparison, there is also an in vivo study, which measured the amount and distribution of forces transmitted across the radioulnocarpal joint under physiological loading conditions by Rikli et al. [61]. The authors found that load transmission across the ulnar column is far greater than previously believed since the lunate transmits load to this entire area [61]. These findings again correspond to the results of the reference model's shift of load distribution towards the lunate.
These parameters are highly subject-specific and hence variations are common among models. Nevertheless, it is assumed that the modeling represents physiological loading well to a reasonable extent for the desired comparison.
Furthermore, an uneven load distribution is the key characteristic of a physiologically RCJ and therefore an assumption of evenly distributed loads on the articular cartilage would greatly simplify the loading mechanism.

4.2 Parameter Sensitivity Study

The parameter sensitivity study performed on the reference model showed various outcomes. First, the largest difference compared to the reference model was present, if no cartilage was used. This appears plausible since a major component in the contact interaction as well as its capability of load distribution were missing. The smaller differences if the cartilage's thickness was decreased or increased, leads to the assumption that the chosen thickness is in a correct range, given the fact that the actual patient-specific cartilage thickness was unknown in this thesis. The findings regarding alterations of the cartilage thickness are supported by the results of Willing et al. [62], which have shown that uniformly increasing and decreasing the cartilage thickness in the elbow joint, changed cartilage contact area and mean contact pressure significantly. Nevertheless, alterations of the cartilage thickness led to certain differences compared to the reference model and one has

to consider these possible factors of error, when establishing such a model. Certainly, this parameter plays a role to some extent, but first and foremost cannot be left out without the risk of a considerably large mistake being made. For this thesis, the error made was kept in consideration since no physiological cartilage thickness was given through the data set.

Second, regarding the changes in the cartilage material type, there was no difference if a hyperelastic material or an elastic material were used. Though, a change in Young's modulus altered the effective stress in cortex and trabecular region. These findings are supported by the work of Carrigan et al. [59], where the authors found that a reduction of the cartilage's Young's modulus from 10MPa to 5MPa resulted in a 23% reduction in peak contact pressure, due to an increase in cartilage deformation, and hence an increase in contact area. Furthermore, the results of this thesis appear plausible, since a decrease in stiffness also reduces the capability of load distribution of the cartilage and hence load transmission to the bone is decreased.

The large difference of hexahedral elements (both, linear and quadratic) compared to tetrahedral elements in the reference model seem to stem from the mesh generation technique used for hexahedral elements. The bottom-up mesh generation of hexahedral elements altered the geometry of the meshed part by reducing the volume of the cartilage by 17.5% (see section 2.2). Therefore, the contact interaction was altered and hence the effective stress in the cortex and trabecular differed. Unfortunately, this alteration of geometry were unavoidable due to the curved geometry of the cartilage and the lack of possibilities to mesh the cartilage in Abaqus differently.

The application of different contact enforcement methods did not change the effective stress substantially and is of minor importance in the establishment of such a model, compared to the other tested parameters.

Hence, it can be stated that contact interaction depends rather on the geometries involved in the contact regions than on the used enforcement methods in this case.

Overall, the reference model was not completely robust in terms of the tested parameters, but based on the calculated errors made between variations, the results were considered acceptable.

4.3 Linearity of Subchondral Bone Stresses

The results of the analysis of subchondral bone stresses in the reference model showed that the model did not scale linearly with an increase of applied load. Overall, there are three sources of nonlinearity present in the model: geometric nonlinearity due to large deformations of the bone, material nonlinearity in the cartilage and BC nonlinearity resulting from the contact interaction of carpal bones and cartilage. Since strains in the

bone were small compared to the ones in the cartilage, geometric nonlinearity due to large deformations of the bone might play a minor part for the subchondral bone stresses. Furthermore, the nonlinear cartilage material did not greatly affect the subchondral bone stresses, because it had been shown in the parameter sensitivity study that there was no difference if a hyperelastic material or an elastic material were used (see section 3.2).
Although, the results showed that nonlinearity was present for all loads applied compared to the 250N of the reference model, this nonlinearity became smaller for load levels of 1000N and 3000N. Therefore, it can be stated that linearly scaling subchondral bone stresses with contact interaction is only valid for certain levels of load, unless a relatively large error is accepted.

4.4 Comparison of Reference Model to Simplified Models

Based on the comparison of the models with simplified BCs and the reference model, the research question could be investigated. The research question was formulated as following: what level of detail regarding the BCs at the RCJ must be used to achieve a realistic representation of stresses in the subchondral and Colles' fracture region?
The qualitative comparison of the contour plots showed that the more complex the applied BCs, the stronger pronounced the stress concentrations in the subchondral trabecular region. If statically equivalent loads were applied, then in the cortex the stresses were represented similarly compared to the reference model for both simplified models (EM and BM). While on the other hand, in the trabecular region stresses in the subchondral and Colles' fracture region were underestimated.
Overall, in all models the stresses in the trabecular region had almost completely decayed before they reached the Colles' fracture region, which is supported by other studies which successfully replicated Colles' fractures by using an embedding experimental setup [40]. This validates the hypothesis of the thesis that simplifications of BCs of RCJ FE models lead to significant changes of bone stresses in the subchondral region, but minor differences in the Colles' fracture region. The hypothesis was further supported since there were local differences in terms of the $NRMSE_{Slice,\ max}$, which was overall lower for all simplified models in the Colles' fracture region compared to the subchondral region.
Uniaxially loaded models did not result in statically equivalent loads and hence stress distribution differed substantially from the reference model. However, the application of statically equivalent loads reduced errors in all simplified models. Therefore, it is crucial to distinguish between different applications of FE models and to interpret the results in the respective context.
If an experimental test is performed to measure the occurring forces in a cadaver model and hence the correct forces and moments could be applied to a model, an EM would

capture the stresses at the level of the Colles' fracture region sufficiently, while a model with carpal bones would greatly reduce the error in the subchondral region.
On the other hand, considering a patient-specific FE model with clinical CT resolution and without an experimental setup or validation, for example. In this setting physiological cartilage thickness cannot be extracted from the data and therefore it seems feasible to fill the articular gap with cartilage, as performed in the BMs. Via this modeling approach the stress distribution in the subchondral trabecular region is represented fairly similar compared to a contact model, but with an underestimation of peak stresses.
However, there always remains a residual error if contact interaction is left out and in particular the subchondral stress peaks can be represented only to a limited extent by simplified models. Therefore, if the local stress distribution in the subchondral region is relevant to the application, modeling contact interaction is necessary.

4.5 Limitations

Several limitations of this work, regarding in particular the available data, have to be discussed. First of all, the available data set used in this work had its limitations in terms of its resolution. With a regular CT data set with an anisotropic voxel size of 1.27x1.27x0.25mm the model was bound to homogeneous isotropic material properties, even though bone is known to be inhomogeneous and orthotropic.
That is because the images were not calibrated in terms of bone mineral density to implement inhomogeneity and clinical CT data is generally insufficient to capture the material orientation necessary to include orthotropic material behavior. In order to include at least the large difference of density in trabecular and cortical regions, they were segmented and modeled separately.
Even though, isotropic resampling of the image data helped with segmentation accuracy, the resolution was still not ideal, which made a complete automated image segmentation impossible, and a slight manual segmentation was necessary, which opened the possibility for user related inaccuracies in the segmentation.
Additionally, the single sample limits the explanatory power of the results and a larger sample size would be needed to clearly show significant differences between the different modeling procedures.
Another limitation of the study is the validation of the reference model, in particular the contact interaction. Although intra-articular pressure measurements have already been performed in vivo by Rikli et al. [61], it is a very complex procedure and beyond the scope of this thesis..
Instead, the contact areas and pressure distribution were compared to in vivo, in vitro as well as FE models from the literature.

Nevertheless, this limitation might not have a large implication on the application of the gathered results, since the main idea of this work was to perform an intra-model comparison with the same radius for all different models, which would otherwise not have been possible.
Since modeling contact interaction in the RCJ is a complex matter and gives rise to underconstraint issues, the BCs were kept as constrained as possible for the sake of simplicity. Although the uniaxial load case might simplify the physiologically correct loading of the carpal bones to some degree, this constraint was chosen to avoid rigid body motion and possible rotation of the carpal bones. Hence, the uniaxial loading with only a single DoF and a vertical force might not represent the most physiological load case, but made a direct comparison with the EM possible.
The error of the BMs compared to the reference model can be explained on the one hand via the contact interaction and on the other hand due to the restrained contact interface of the carpal bones with the cartilage. Since the cartilage was modeled with predefined area of contact with the carpal bones, this has certainly influenced the seating of the carpal bones and therefore the load transmission. Nevertheless, this was unavoidable using this method of filling the articular gap with cartilage.

4.6 Conclusion

A reference model of the distal radius with articular loading was established and tested for its robustness against changes of parameters. The qualitative comparison between models with simplified BCs and the reference model showed that the more complex the applied BCs, the stronger pronounced the stress concentrations in the subchondral trabecular region. If statically equivalent loads were applied, stresses in the cortex were represented similarly compared to the reference model for both simplified models (EM and BM), while stresses in the subchondral and Colles' fracture region of the trabecular were underestimated. The comparison of this reference model with models of reduced complexity regarding their BCs showed that the type of application is essential for choosing the correct modeling approach. It can be stated that, if correct reaction forces and moments are known and the region of interest lies within the Colles' fracture region, a large simplification of BCs such as in the EMs can be utilized. If the stress distribution in the subchondral region is of interest, the application of statically equivalent loads and load transmission through carpal bones do not represent stress peaks sufficiently compared to a contact model and an error is unavoidable.

Bibliography

[1] K. W. Nellans, E. Kowalski, and K. C. Chung. “The Epidemiology of Distal Radius Fractures”. In: *Hand Clinics* 28(2) (2012), pp. 113–125.

[2] S. F. Baumbach, R. Schmidt, P. Varga, T. Heinz, V. Vécsei, and P. K. Zysset. “Where is the distal fracture line location of dorsally displaced distal radius fractures?” In: *Journal of Orthopaedic Research* 29(4) (2011), pp. 489–494.

[3] S. Quadlbauer, C. Pezzei, J. Jurkowitsch, R. Rosenauer, B. Kolmayr, T. Keuchel, D. Simon, T. Beer, T. Hausner, and M. Leixnering. “Rehabilitation after distal radius fractures: is there a need for immobilization and physiotherapy?” In: *Archives of Orthopaedic and Trauma Surgery* 140(5) (2020), pp. 651–663.

[4] I. Mehling, L. P. Müller, K. Delinsky, D. Mehler, D. Ing, K. J. Burkhart, and P. M. Rommens. “Number and Locations of Screw Fixation for Volar Fixed-Angle Plating of Distal Radius Fractures: Biomechanical Study”. In: *The Journal of Hand Surgery* 35(6) (2010), pp. 885–891.

[5] M. E. Muller, C. E. Webber, and M. L. Bouxsein. “Predicting the failure load of the distal radius”. In: *Osteoporosis International* 14(4) (2003), pp. 345–352.

[6] W. B. Edwards and K. L. Troy. “Finite element prediction of surface strain and fracture strength at the distal radius”. In: *Medical Engineering and Physics* 34(3) (2011), pp. 290–298.

[7] J. A. MacNeil and S. K. Boyd. “Bone strength at the distal radius can be estimated from high-resolution peripheral quantitative computed tomography and the finite element method”. In: *Bone* 42(6) (2008), pp. 1203–1213.

[8] J. E. Johnson and K. L. Troy. “Simplified boundary conditions alter cortical-trabecular load sharing at the distal radius; A multiscale finite element analysis”. In: *Journal of Biomechanics* 66 (2018), pp. 180–185.

[9] W. B. Edwards and K. L. Troy. “Simulating distal radius fracture strength using biomechanical tests: A modeling study examining the influence of boundary conditions”. In: *Journal of Biomechanical Engineering* 133(11) (2011), pp. 114501-1–5.

[10] J. E. Johnson and K. L. Troy. “Validation of a new multiscale finite element analysis approach at the distal radius”. In: *Medical Engineering and Physics* 44 (2017), pp. 16–24.

[11] K. J. Bathe. *Finite Element Procedures*. 2nd. New Jersey: Prentice Hall, 1996. ISBN: 0133014584.

[12] K. H. Yang. *Basic finite element method as applied to injury biomechanics*. Elsevier Inc., 2017. ISBN: 9780128098325.

[13] L. De Lorenzis, P. Wriggers, and C. Weißenfels. *Computational Contact Mechanics with the Finite Element Method*. 2017. ISBN: 9781119176817.

[14] A. Khennane. *Introduction to finite element analysis using MATLAB® and abaqus*. Baton Rouge: CRC Press, 2013. ISBN: 9781466580213.

[15] M. Smith. *ABAQUS/Standard User's Manual, Version 6.9*. Providence, RI: Dassault Systemes Simulia Corp, 2009.

[16] V. A. Yastrebov. *Introduction to Computational Contact Mechanics*. Paris, 2010.

[17] P. Wriggers. *Computational contact mechanics*. 2nd. Heidelberg: Springer-Verlag, 2006. ISBN: 3540326081.

[18] A. Francavilla and O. C. Zienkiewicz. “A note on numerical computation of elastic contact problems”. In: *International Journal for Numerical Methods in Engineering* 9 (1975), pp. 913–924.

[19] J. C. Simo, P. Wriggers, and R. L. Taylor. “A perturbed Lagrangian formulation for the finite element solution of contact problems”. In: *Computer Methods in Applied Mechanics and Engineering* (1985).

[20] J. Fänghanel, F. Pera, F. Anderhuber, and R. Nitsch. *Waldeyer - Anatomie des Menschen*. 17th. Berlin: De Gruyter, 2003.

[21] M. Schünke, E. Schulte, U. Schumacher, M. Voll, and K. H. Wesker. *Prometheus Allgemeine Anatomie und Bewegungssystem*. 2nd ed. Stuttgart: Georg Thieme Verlag, 2007. ISBN: 9783131395221.

[22] E. Hamed, Y. Lee, and I. Jasiuk. “Multiscale modeling of elastic properties of cortical bone”. In: *Acta Mechanica* 213 (2010), pp. 131–154.

[23] C. R. Ethier. *Introductory biomechanics from cells to organisms*. Cambridge texts in biomedical engineering. Cambridge ; Cambridge University Press, 2007.

[24] J. Smith, William and Hashemi. *Foundations of Materials Science and Engineering*. 6th. New York: McGraw-Hill Education, 2018. ISBN: 978-1-259-69655-8.

[25] S. C. Cowin. *Bone Mechanics Handbook*. 2nd ed. Boca Raton: CRC Press LLC, 2001. ISBN: 9781420036589.

[26] L. S. Levin, J. C. Rozell, and N. Pulos. "Distal radius fractures in the elderly". In: *Journal of the American Academy of Orthopaedic Surgeons* 25(3) (2017), pp. 179–187.

[27] H. E. Huetteman, M. J. Shauver, S. Malay, T. T. Chung, and K. C. Chung. "Variation in the treatment of distal radius fractures in the United States: 2010 to 2015". In: *Plastic and Reconstructive Surgery* 143(1) (2019), pp. 159–167.

[28] M. McQueen and J. Caspers. "Colles fracture: Does the anatomical result affect the final function?" In: *Journal of Bone and Joint Surgery - Series B* 70(4) (1988), pp. 649–651.

[29] aap Implants Inc. *Loqteq - Distal Radius and Ulna Plates - Surgical Technique*. Tech. rep. Atlanta, 2021, p. 26.

[30] A. J. C. B. Saint-Venant. "Memoire sur la Torsion des Prismes". In: *Mem. Divers Savants* 14 (1855), pp. 233–560.

[31] G. Ducher, S. Prouteau, D. Courteix, and C. L. Benhamou. "Cortical and trabecular bone at the forearm show different adaptation patterns in response to tennis playing". In: *Journal of Clinical Densitometry* 7(4) (2004), pp. 399–405.

[32] P. Schneider, C. Reiners, G. R. Cointry, R. F. Capozza, and J. L. Ferretti. "Bone quality parameters of the distal radius as assessed by pQCT in normal and fractured women". In: *Osteoporosis International* 12(8) (2001), pp. 639–646.

[33] J. A. Spadaro, F. W. Werner, R. A. Brenner, M. D. Fortino, L. A. Fay, and W. T. Edwards. "Cortical and trabecular bone contribute strength to the osteopenic distal radius". In: *Journal of Orthopaedic Research* 12(2) (1994), pp. 211–218.

[34] R. Oftadeh, M. Perez-Viloria, J. C. Villa-Camacho, A. Vaziri, and A. Nazarian. "Biomechanics and Mechanobiology of Trabecular Bone: A Review". In: *Journal of Biomechanical Engineering* 137(1) (2015), pp. 010802-1–5.

[35] H. Y. K. Cheng, C. L. Lin, Y. H. Lin, and A. C. Y. Chen. "Biomechanical evaluation of the modified double-plating fixation for the distal radius fracture". In: *Clinical Biomechanics* 22(5) (2007), pp. 510–517.

[36] Y. H. Lin, C. L. Lin, H. N. Kuo, M. T. Sun, and A. C. Y. Chen. "Biomechanical analysis of volar and dorsal double locking plates for fixation in comminuted extra-articular distal radius fractures: A 3D finite element study". In: *Journal of Medical and Biological Engineering* 32(5) (2012), pp. 349–356.

[37] A. Ural. "Prediction of Colles' fracture load in human radius using cohesive finite element modeling". In: *Journal of Biomechanics* 42(1) (2009), pp. 22–28.

[38] A. Synek, Y. Chevalier, S. F. Baumbach, and D. H. Pahr. "The influence of bone density and anisotropy in finite element models of distal radius fracture osteosynthesis: Evaluations and comparison to experiments". In: *Journal of Biomechanics* 48(15) (2015), pp. 4116–4123.

[39] W. Pistoia, B. Van Rietbergen, E. M. Lochmüller, C. A. Lill, F. Eckstein, and P. Rüegsegger. "Estimation of distal radius failure load with micro-finite element analysis models based on three-dimensional peripheral quantitative computed tomography images". In: *Bone* 30(6) (2002), pp. 842–848.

[40] P. Varga, D. H. Pahr, S. Baumbach, and P. K. Zysset. "HR-pQCT based FE analysis of the most distal radius section provides an improved prediction of Colles' fracture load in vitro". In: *Bone* 47(5) (2010), pp. 982–988.

[41] S. I. f. C. A. Surgery. *SMIR - SICAS Medical Image Repository*. 2020.

[42] R. Kikinis, S. D. Pieper, and K. G. Vosburgh. "3D Slicer: A Platform for Subject-Specific Image Analysis, Visualization, and Clinical Support". In: *Intraoperative Imaging and Image-Guided Therapy*. Springer New York, 2014, pp. 277–289.

[43] 3DSlicer.org. *3D Slicer Wiki Pages*. 2021.

[44] C. Tomasi and R. Manduchi. "Bilateral filtering for gray and color images". In: *Proceedings of the IEEE International Conference on Computer Vision*. IEEE, 1998, pp. 839–846.

[45] 3DSlicer.org. *Slicer Read the Docs - Segment Editor*. 2021.

[46] T. M. Bücking, E. R. Hill, J. L. Robertson, E. Maneas, A. A. Plumb, and D. I. Nikitichev. "From medical imaging data to 3D printed anatomical models". In: *PLOS ONE* 12(5) (2017). Ed. by H.-C. I. Chen, e0178540.

[47] G. Wu, F. C. Van Der Helm, H. E. Veeger, M. Makhsous, P. Van Roy, C. Anglin, J. Nagels, A. R. Karduna, K. McQuade, X. Wang, F. W. Werner, and B. Buchholz. "ISB recommendation on definitions of joint coordinate systems of various joints for the reporting of human joint motion - Part II: Shoulder, elbow, wrist and hand". In: *Journal of Biomechanics* 38(5) (2005), pp. 981–992.

[48] J. Pollock, R. V. O'Toole, S. D. Nowicki, and W. A. Eglseder. "Articular cartilage thickness at the distal radius: A cadaveric study". In: *Journal of Hand Surgery* 38(8) (2013), pp. 1477–1481.

[49] S. A. Maas, B. J. Ellis, D. S. Rawlins, and J. A. Weiss. "Finite element simulation of articular contact mechanics with quadratic tetrahedral elements". In: *Journal of Biomechanics* 49(5) (2016), pp. 659–667.

[50] P. Varga, P. Schefzig, E. Unger, W. Mayr, P. K. Zysset, and J. Erhart. "Finite element based estimation of contact areas and pressures of the human scaphoid in various functional positions of the hand". In: *Journal of Biomechanics* 46(5) (2013), pp. 984–990.

[51] L. W. Marks and T. N. Gardner. "The use of strain energy as a convergence criterion in the finite element modelling of bone and the effect of model geometry on stress convergence". In: *Journal of Biomedical Engineering* 15(6) (1993), pp. 474–476.

[52] U. M. Ayturk and C. M. Puttlitz. "Parametric convergence sensitivity and validation of a finite element model of the human lumbar spine". In: *Computer Methods in Biomechanics and Biomedical Engineering* 14(8) (2011), pp. 695–705.

[53] C. G. Armstrong, W. M. Lai, and V. C. Mow. "An analysis of the unconfined compression of articular cartilage". In: *Journal of Biomechanical Engineering* 106(4) (1984), pp. 165–173.

[54] P. Christen, K. Ito, I. Knippels, R. Müller, G. H. van Lenthe, and B. van Rietbergen. "Subject-specific bone loading estimation in the human distal radius". In: *Journal of biomechanics* 46(4) (2013), pp. 759–766.

[55] D. P. Fyhrie and D. R. Carter. "A unifying principle relating stress to trabecular bone morphology". In: *Journal of Orthopaedic Research* 4(3) (1986), pp. 304–317.

[56] R. Eastell, H. W. Wahner, M. O'Fallon, P. C. Amadio, L. J. Melton, and B. L. Riggs. "Unequal decrease in bone density of lumbar spine and ultradistal radius in Colles' and vertebral fracture syndromes". In: *Journal of Clinical Investigation* 83(1) (1989), pp. 168–174.

[57] M. Majima, E. Horii, H. Matsuki, H. Hirata, and E. Genda. "Load Transmission Through the Wrist in the Extended Position". In: *Journal of Hand Surgery* 33(2) (2008), pp. 182–188.

[58] D. D. Anderson, B. R. Deshpande, T. E. Daniel, and M. E. Baratz. "A three-dimensional finite element model of the radiocarpal joint: distal radius fracture step-off and stress transfer." In: *Iowa Orthopedic Journal* 25 (2005), pp. 108–117.

[59] S. D. Carrigan, R. A. Whiteside, D. R. Pichora, C. F. Small, and K. G. Hospital. "Development of a three-dimensional finite element model for carpal load transmission in a static neutral posture". In: *Annals of Biomedical Engineering* 31(6) (2003), pp. 718–725.

[60] J. E. Johnson, T. E. Mciff, P. Lee, E. Bruce Toby, K. J. Fischer, and E. B. Toby. "Validation of radiocarpal joint contact models based on images from a clinical MRI scanner NIH Public Access". In: *Comput Methods Biomech Biomed Engin* 17(4) (2014), pp. 378–387.

[61] D. A. Rikli, P. Honigmann, R. Babst, A. Cristalli, M. M. Morlock, and T. Mittlmeier. "Intra-Articular Pressure Measurement in the Radioulnocarpal Joint Using a Novel Sensor: In Vitro and In Vivo Results". In: *Journal of Hand Surgery* 32(1) (2007), pp. 67–75.

[62] R. T. Willing, E. A. Lalone, H. Shannon, J. A. Johnson, and G. J. King. "Validation of a finite element model of the human elbow for determining cartilage contact mechanics". In: *Journal of Biomechanics* 46(10) (2013), pp. 1767–1771.

Supplementary Figures

In the following the remaining qualitative results of the parameter sensitivity study (see section 3.2) showing the effects of different cartilage material types (see Figure S1), cartilage element types (see Figure S2) and contact enforcement methods (see Figure S3) on the effective stresses and the contact pressure of the reference model are presented.
As mentioned in the results section, a change in Young's modulus from 10MPa to 5MPa led to a considerably small change, while changing the material from an elastic to a hyperelastic material on the other hand, showed almost no differences in the effective stresses.
In terms of a change of the used element type for modeling the cartilage, the use of hexahedral elements resulted in the largest difference. A change to linear elements (C3D4 and C3D8) showed larger stress peaks in the contact area of the lunatum. Both hexahedral element types (C3D8 and C3D20) showed smaller involvements of the scaphoid in the contact interaction.
Regarding the use of different contact enforcement methods there was also no differences visible in the qualitative contour plots of the effective stresses or contact pressure.

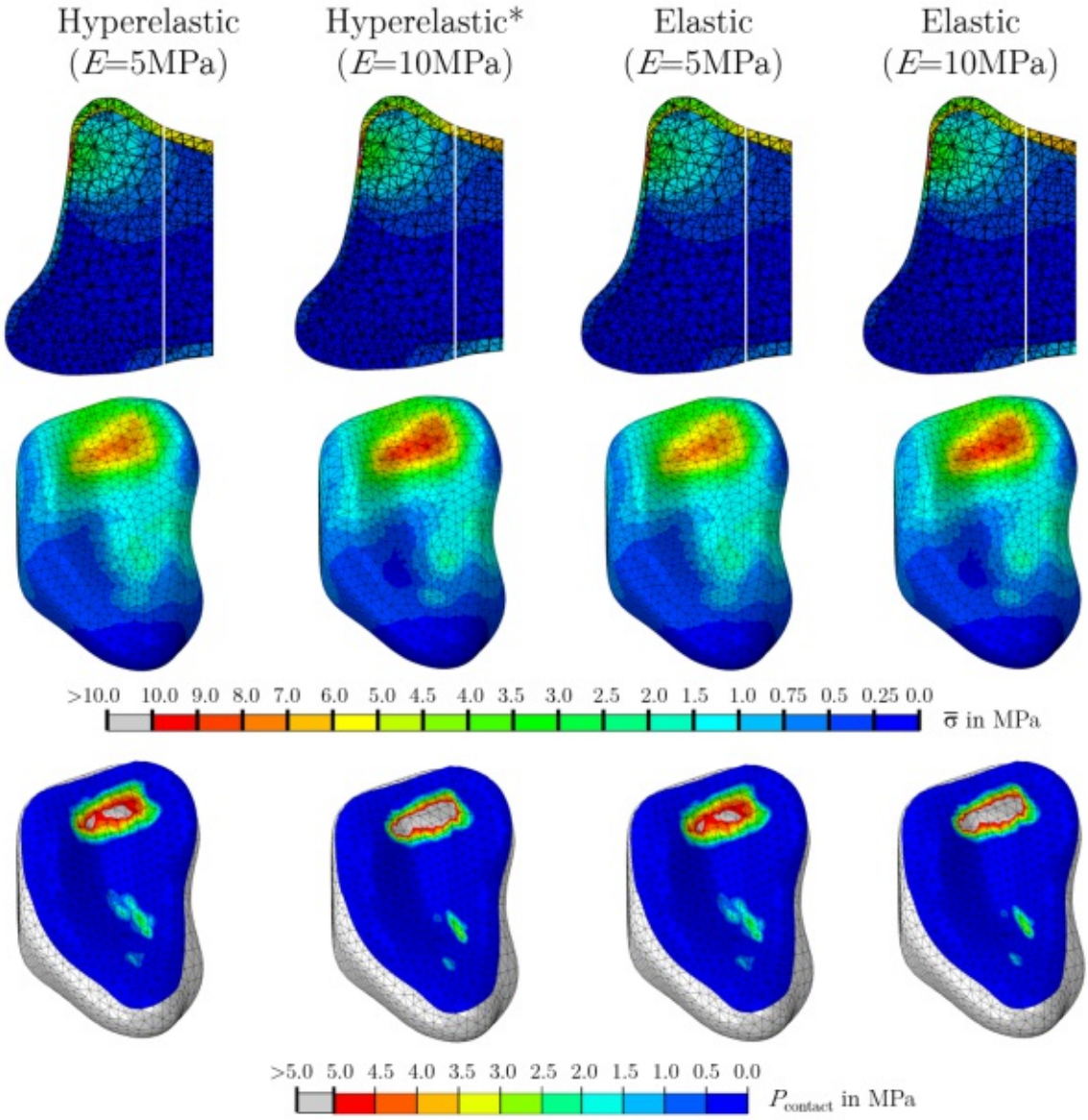

Figure S1: Qualitative contour plots of the effective stress ($\bar{\sigma}$) in MPa of the models with hyperelastic (5MPa), hyperelastic (10MPa) (=reference model), elastic (5MPa) and elastic (10MPa) material properties. The top row shows the view cut of the z-y-plane including the subchondral as well as the Colles' fracture region. The second row shows the view of the articular surface of the bone. The third row displays the contact pressure on the cartilage.

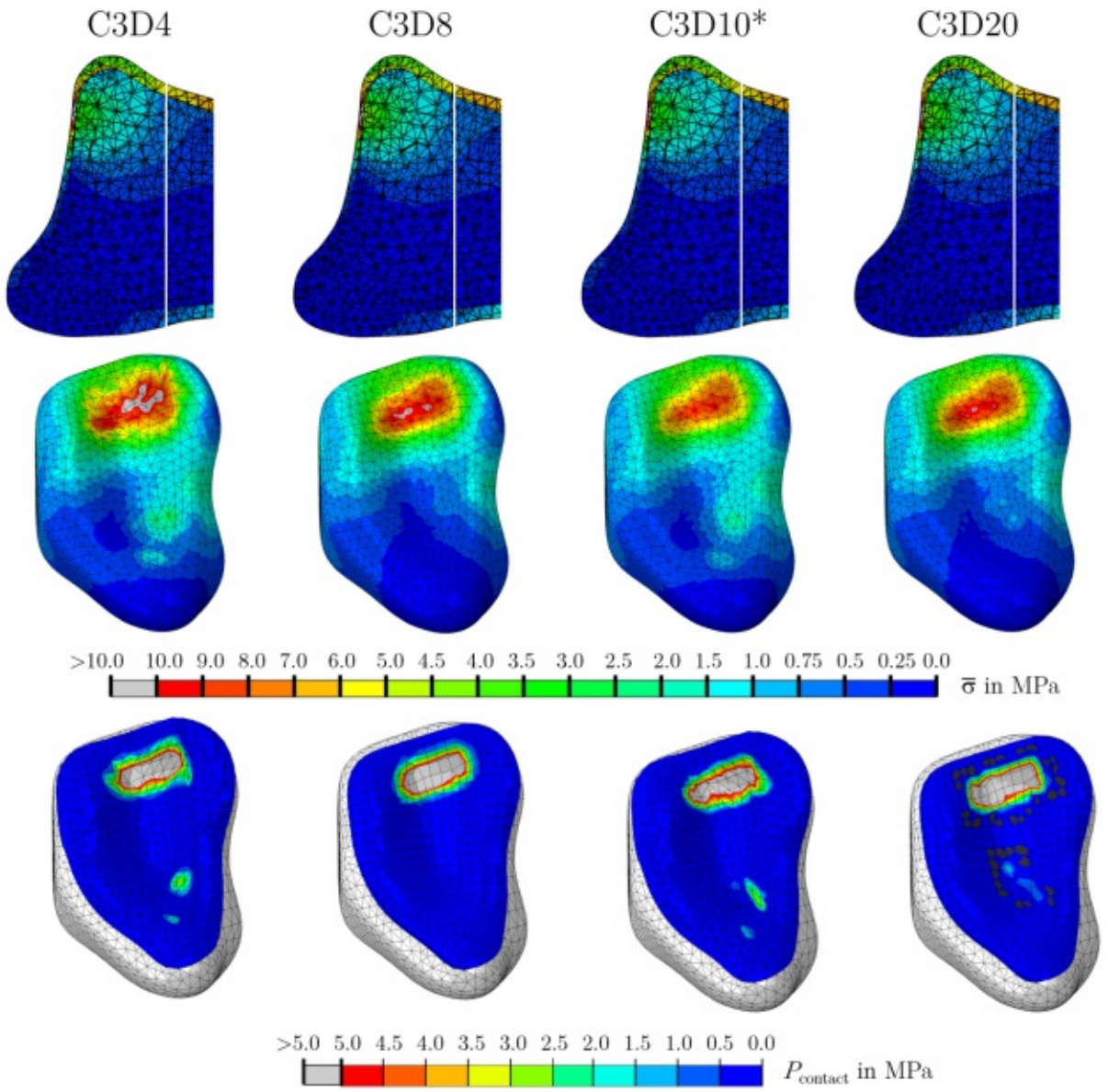

Figure S2: Qualitative contour plots of the effective stress ($\bar{\sigma}$) in MPa of the models with C3D4, C3D8, C3D10 (=reference model) and C3D20 element types. The top row shows the view cut of the z-y-plane including the subchondral as well as the Colles' fracture region. The second row shows the view of the articular surface of the bone. The third row displays the contact pressure on the cartilage. The black color of certain elements in the contour plot of the contact pressure of the quadratic hexahedral elements could not be explained and was considered as a visual artifact, since pressure values were present according to the color scale.

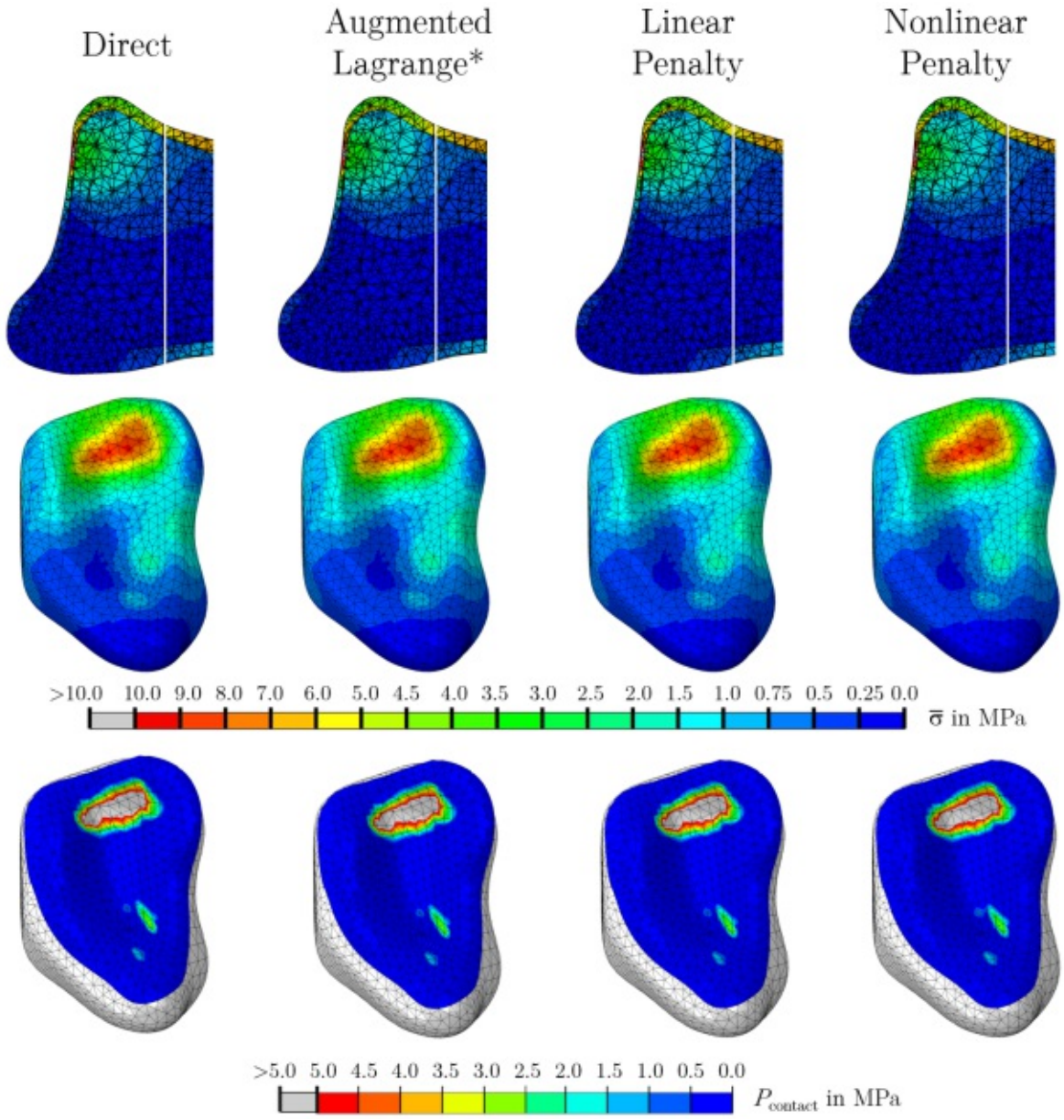

Figure S3: Qualitative contour plots of the effective stress ($\bar{\sigma}$) in MPa of the models with different contact enforcement methods (direct, augmented Lagrange (=reference model), linear penalty and nonlinear penalty. The top row shows the view cut of the z-y-plane including the subchondral as well as the Colles' fracture region. The second row shows the view of the articular surface of the bone. The third row displays the contact pressure on the cartilage.